Materials Advances

ROYAL SOCIETY OF CHEMISTRY

PAPER

View Article Online
View Journal | View Issue

Cite this: *Mater. Adv.*, 2025, **6**, 3686

Tuning the antimicrobial and photocatalytic activity of nano-ZnO by metal doping†

Md. Atikur Rahman,[ab] Md. Tanvir Hossain,[b] Md Farid Ahmed,[a] Muhammad Shahriar Bashar,[c] Subarna Sandhani Dey,[d] Samina Ahmed *[a] and Md. Sahadat Hossain *[a]

The uncontrolled discharge of hospital and pharmaceutical waste pollutes aquatic ecosystems by introducing diverse microorganisms and drug-resistant pathogens that later affect human health, while the release of toxic dyes from textile industries further harms the ecosystem. Nanomaterials, with their multifunctional properties, provide effective solutions for degrading dyes and eliminating harmful microorganisms. In this work, an inexpensive and simple chemical precipitation method was adopted to prepare pure ZnO and $Zn_{1-x}M_xO$ nanoparticles doped with metals where M = Ag, Cu, Co, Fe, and Ca, with x set at 0.5. The produced materials were evaluated using a variety of techniques, including XRD, TEM, SEM, and DLS. The results showed that the particle sizes ranged from 92 to 129 nm for all samples, with hydrodynamic diameters of 293 nm for PZO and 383 nm for AgZO. FTIR analysis was used to confirm the formation of Zn–O bonds and assess the purity of the samples. AgZO exhibited significant antibacterial activity among all samples, targeting Gram-positive strains such as *B. cereus*, *L. monocytogenes*, and *S. aureus*, along with Gram-negative *E. coli*, producing inhibition zones of 10.2 ± 0.35 mm, 11.2 ± 0.29 mm, 10.2 ± 0.29 mm, and 20.8 ± 0.80 mm, respectively. The photocatalytic efficiency in degrading 10 ppm Congo Red (CR) dye reached approximately 95.17%, 94.81%, and 94.81% for CuZO, AgZO, and PZO samples, respectively. The nearly identical band gap energy indicates that the photocatalytic activity of PZO and AgZO NPs is comparable.

Received 6th February 2025,
Accepted 17th April 2025

DOI: 10.1039/d5ma00101c

rsc.li/materials-advances

1. Introduction

Rapid and reckless urbanization and industrialization plans resulted in a major rise in environmental pollution, with textile and pharmaceutical wastes being the most hazardous. Reducing the impact of these industries is crucial in addressing aquatic and air pollution, particularly in terms of lowering the chemical oxygen demand (COD) and bio-chemical oxygen demand (BOD), due to the release of various microorganisms in freshwater reservoirs and reduced light penetration for the photosynthesis process resulting from human activities.[1] In addition to their high toxicity and carcinogenic nature, the dyes and microorganisms could influence genomic mutations in aquatic plants and potentially integrate into the food chain.[2] Congo red (CR) is regarded as one of the most dangerous dyes, as its partial degradation generates harmful aromatic substances that are classified as carcinogenic, mutagenic, and teratogenic agents.[3] So, degrading dye solutions is essential for safeguarding aquatic biota and humans, necessitating the development of efficient methods to diminish their toxic concentrations in water.

In 2019, the World Health Organization identified the most pressing global health dangers, including antibiotic resistance, a probable global influenza epidemic, and other infection-related disorders being among the top worries.[4] Bacterial infections result in the loss of numerous lives every year, while influenza pandemics severely affect both health systems and economic stability worldwide.[5] Since Fleming's groundbreaking discovery of antibiotics in 1928, their excessive and improper application has resulted in the development of resistant microorganisms, a critical public health issue linked to an estimated 700 000 deaths annually.[6] By 2050, around 10 million deaths annually are anticipated to result from bacteria that are resistant to antibiotics.[7] To tackle these challenges related to health and the environment, researchers view nanoparticles as a significant solution owing to their multifunctional properties.

[a] *Institute of Glass & Ceramic Research and Testing, Bangladesh Council of Scientific and Industrial Research (BCSIR), Dhaka-1205, Bangladesh. E-mail: shanta_samina@yahoo.com, saz8455@gmail.com*
[b] *Department of Applied Chemistry and Chemical Engineering, Noakhali Science and Technology University, Noakhali, Bangladesh*
[c] *Institute of Energy Research & Development, Bangladesh Council of Scientific and Industrial Research (BCSIR), Dhaka 1205, Bangladesh*
[d] *Institute of Food Science and Technology (IFST), Bangladesh Council of Scientific and Industrial Research (BCSIR), Dhaka, Bangladesh*

† Electronic supplementary information (ESI) available. See DOI: https://doi.org/10.1039/d5ma00101c

A large spectrum of nanoparticles have been applied in the past few decades to overcome this situation, such as ZnO,[8] CuO,[9] TiO_2,[10] Fe_3O_4,[11] g-C_3N_4,[12] and others.

The US FDA (21CFR182.8991) has identified five zinc-based compounds as secure and potent antibacterial agents, including ZnO nanostructures.[13] Within the field of electrochemistry, ZnO finds diverse applications, including its recent utilization in the development of an electrochemical sensor for acetone detection, achieving a detection limit of 0.03 ppm.[14] Acting as both an antioxidant and a catalyst, ZnO NPs contribute to formic acid dehydrogenation, yielding hydrogen gas through a simple and cost-efficient method.[15]

ZnO nanoparticles (ZnO-NPs) have emerged as a leading choice for photocatalysts due to their distinctive characteristics, including having a direct band-gap (3.37 eV), being non-toxic and safe, having a high binding energy of 60 meV for activation, and exhibiting fast electron mobility and strong oxidation capability.[16] Its wide band gap limits its application by absorbing mostly UV light, and it exhibits point defects like oxygen vacancies.[17] Moreover, pure ZnO-NPs' photocatalytic efficacy is greatly reduced by the constant recombination of electrons and holes.[18] Therefore, modifying ZnO by doping it with different metals is a highly effective strategy for resolving these challenges. By decreasing the band gap, doping with metals like Ag and Cu increases photocatalytic activity.[8] Doped ZnO NPs exhibit surface plasmon resonance, enabling them to absorb electromagnetic energy and facilitate the creation of electron–hole pairs.[19] To minimize expenses, this research employs affordable metal nitrate salts, such as nitrates of Ag, Cu, Co, Fe and Ca, as alternatives to costly metals. ZnO-NPs can be produced using various techniques, including precipitation,[20] co-precipitation,[21] sol–gel,[22] hydrothermal,[23] green synthesis,[24] microwave-assisted synthesis,[25] physical vapor deposition (PVD),[26] mechanical milling,[27] and laser ablation.[28] Nanoparticles like ZnO effectively transfer electrons after absorbing light energy, enabling electron transitions from the valence band to the conduction band and forming holes. The interaction of electrons and holes with water and hydroxyl ions generates additional free radicals ($^{\bullet}OH$), which degrade organic bonds and eliminate dyes through redox reactions.[29] Bacteria, being porous and micrometer-sized, are easily infiltrated by nanoparticles, which generate reactive oxygen species (ROS), release Zn^{2+} ions, and accumulate within the cells, inhibiting protein formation and leading to cell death.[30]

In this study, the chemical precipitation method was chosen as the synthesis approach because of its affordability, simplicity, operational ease, scalability, exact control of particle size and shape, as well as the synthesis of materials that are crystalline and highly pure. Each sample was doped with 0.5% metal concentration, and multiple characterization techniques were utilized to study the crystal size, shape, optical properties, and morphologies of pure and doped ZnO-NPs, which exhibited remarkable photocatalytic and antimicrobial properties. Although individual studies have explored these metals separately or in subsets, the integration of Ag, Cu, Co, Fe, and Ca with ZnO-NPs into one comprehensive analysis remains unaddressed in the current literature. Comparing all five metal-doped ZnO nanoparticles is easier than analyzing them individually. This paper aims to evaluate and compare various metal-doped ZnO-NPs, focusing on less explored aspects in the literature.

2. Methods and materials

2.1. Materials

The most frequently used chemical, 96% pure Zn-nitrate hexahydrate [$Zn(NO_3)_2{\cdot}6H_2O$], was employed to synthesize pure and various metal-doped ZnO-NP samples, purchased from Loba Chemie Pvt. Ltd, India, and nitrate salts of Ag (99%, Sigma-Aldrich), Cu (95%, Loba Chemie), Ca (Millipore Sigma, Germany), Co (97%, Merck, India), and Fe (Research lab Chem. Industry, India) were used as dopant salts to supply the dopant metals. NaOH (commercial grade) and deionized water (DI) were used in every synthesis process.

2.2. Synthesis of ZnO nanoparticles

A simple and inexpensive chemical precipitation method has been utilized for fabricating ZnO-NPs. ZnO nanocrystals were formed by dissolving Zn-nitrate hexahydrate (10 mM) in 50 mL of DI water under continuous stirring. Once the salt had completely dissolved, the temperature was increased to 70 °C, and then 4 M NaOH was added (0.5 mL min^{-1}) from a burette until the pH reached 12. Under these circumstances, the precipitate developed and was kept for two hours. This was followed by filtering and cleaning the precipitate three times with DI water and once with ethanol. Ultimately, the powder was dried using a vacuum dryer set at 45 °C overnight and calcined at 500 °C for 4 h.

For the synthesis of doped ZnO NPs, a 0.5 mol% dopant salt ($Zn_{1-x}M_xO$) is used, where x = 0.5 and M = Ag, Cu, Ca, Co, and Fe. Specifically, for the synthesis of Ag-doped ZnO NPs, 0.5 mol% $AgNO_3$ (relative to zinc nitrate hexahydrate) is combined with an appropriate amount of zinc salt in a beaker and stirred for 30 minutes. Then, the same technique is repeatedly applied for the synthesis of ZnO-NPs doped with other metals by changing metal precursors only. In this research, the synthesized samples of pure ZnO and ZnO doped with 0.5% of Ag, Cu, Co, Fe, and Ca were labeled as PZO, AgZO, CuZO, CoZO, FeZO, and CaZO, respectively (Fig. 1).

2.3. Characterization

2.3.1. X-ray diffraction analysis. The synthesized samples' X-ray diffractogram was obtained using the Rikagu SE XRD system, which operated at 40 kV and 50 mA while maintaining a cooling water temperature of 20 to 30 °C. The device's X-ray source was copper, producing a wavelength of 1.5406 Å, and measurements were recorded in 0.01 increments across the 2θ range of 10–70°. A nickel shield was positioned in front of the detector to obstruct beta radiation from the X-ray source, and before the analysis, a calibrated silicon reference was used. Every verified data collection has been analyzed based on

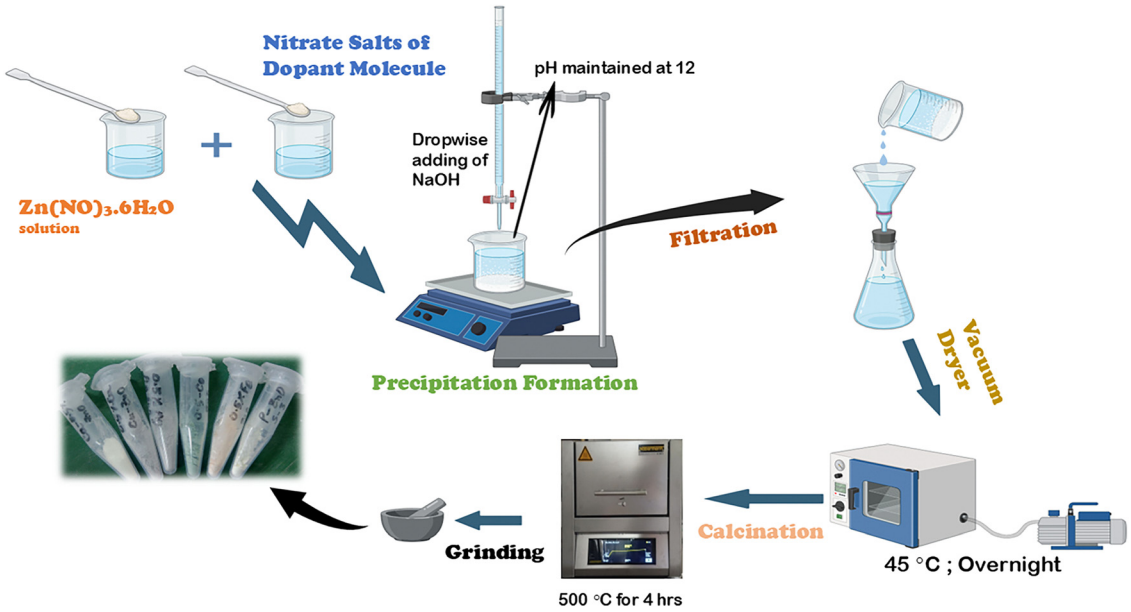

Fig. 1 Schematic diagram of the chemical precipitation method for synthesizing pure and various metal doped ZnO-NPs.

the standards specified by the ICDD database (card no. # 00-036-1451).

2.3.2. FTIR analysis. An IR-prestige 21 FTIR spectrophotometer (Shimadzu, Japan) with an attenuated total reflection (ATR) system was used to examine the distinctive functional groups of ZnO-NPs as well as any possible contaminants. With a spectral bandwidth of 4 cm^{-1}, the FTIR spectrum was obtained from 400 to 4000 cm^{-1}, with an average of 30 scans per sample. All measurements were made under constant conditions at 25 °C and 60% relative humidity.

2.3.3. FESEM analysis. Using a JEOL-JSM-7600F high-resolution field emission scanning electron microscope (FESEM) equipped with an energy dispersive X-ray (EDX) system, pure ZnO-NPs and those doped with various metals were subjected to microstructural and elemental composition analyses. To capture the images, a 15 kV acceleration voltage was employed.

2.3.4. Photocatalytic activity. When a material is exposed to light, often visible or ultraviolet light, it produces electron–hole pairs that accelerate chemical reactions and generate various free radicals. The material is then called a photocatalyst. When catalysts such as ZnO-NPs are exposed to light, their electrons shift from the valence band to the conduction band. This excitation promotes the interactions of electrons with water and oxygen, which results in the production of reactive radicals such as $OH^{\bullet}$, $O_2^{\bullet}$, and $HO_2^{\bullet}$.[31] The experiment was carried out in a 100 mL beaker with 0.07 g of pure and different metal doped-ZnO photocatalyst samples suspended in 40 mL of a CR solution with a concentration of 10.0 mg L^{-1}. A 500 W halogen lamp was placed 65 cm away from the beaker. Eqn (1) and (2) were used to determine photocatalytic degradation and capacity, respectively, where V stands for the volume of the dye solution, W is the sample weight in grams (g), and C_0 and C_t are the starting and ultimate dye concentrations. The absorbance of a specific volume of CR solution was periodically measured, and the sampled portion was then transferred to the degradation medium.

$$\text{Degradation percentage, } D_p = \frac{C_0 - C_t}{C_0} \times 100 \quad (1)$$

$$\text{Degradation capacity, } D_c = \frac{C_0 - C_t}{W} \times V \quad (2)$$

2.3.5. Antibacterial activity

2.3.5.1. Sample preparation. An antibacterial activity test was performed on four bacteria such as *Bacillus cereus* ATCC 11778, *Listeria monocytogenes* ATCC 13932, *Staphylococcus aureus* ATCC 6538, and *Escherichia coli* ATCC 25922, using the produced ZnO-NPs. To perform the test, 40 mg of six ZnO-NP samples was dissolved in distilled water containing 2% Tween 20 (Promega, USA). In the case of well diffusion assay, a sample concentration of 40 mg mL^{-1} was directly applied to the well and to determine the MIC and MBC values eight different concentrations (0.157–20 mg mL^{-1}) of the sample were analyzed against the previously mentioned four bacteria.

2.3.5.2. Antibacterial assay. A well diffusion approach was used to test the ZnO-NPs' antibacterial activity. Inoculums of bacteria were made according to the 0.5 McFarland standard (1×10^7–1×10^8 CFU per mL). A sterile cotton bar was used to equally distribute 100 μL of each bacterial culture in a Mueller–Hinton agar (MHA) plate (HiMedia, India), and a sterile borer was used to create a hole 6 mm in diameter. The plates were incubated for 16–18 hours at 37 °C after 50 μL of each sample (concentration: 40 mg mL^{-1}) was injected into the wells against four microorganisms. Following the guidelines set forth by the Clinical and Laboratory Standards Institute (CLSI, 2020), the

procedure was carried out using distilled water (containing 2% Tween 20) serving as the negative control and 100 ppm of the antibacterial medicine chloramphenicol as the positive control. The zone of inhibition was measured in millimeters (mm) and the assay was performed in triplicate.

2.3.5.3. Minimum inhibitory concentration (MIC) and minimum bactericidal concentration (MBC) assays. The standard tube dilution (CLSI M-07-A8) method was used to determine the minimum bactericidal concentration (MBC) and minimum inhibitory concentration (MIC) of six synthesized ZnO-NPs. The samples were serially diluted (two-fold) from stock solution (40 mg mL^{-1}) and the concentration range was 0.157 to 20 mg mL^{-1}. Gram-negative bacteria, such as *E. coli*, and Gram-positive bacteria, such as *B. cereus*, *L. monocytogenes*, monocytogenes and *S. aureus*, were tested for MIC and MBC values. This study was carried out by serially diluting 100 μL of the sample in distilled water (with 2% Tween 20) and then adding 100 μL of sterile LB media and 10 μL of bacterial suspension (10^{12} CFU per mL) to each tube. After that, the tubes were incubated for 24 hours at 37 °C, and the MIC was determined by measuring the sample's minimal concentration (mg mL^{-1}) at which no apparent microbial growth occurred.[32,33]

For MBC determination, 50 μL of the sample from the tubes with no visible growth on MIC assay were taken and cultured on MHA agar plates. After 24 h at 37 °C the colonies are examined and counted. The MBC endpoint is defined as the sample concentration at which 99.9% of the bacteria were destroyed.[34]

3. Results and discussion

3.1. Crystal phase analysis

As illustrated in Fig. 2, the X-ray diffractograms of pure ZnO and multiple metal-doped ZnO nanoparticles ($Zn_{1-x}M_xO$) exhibit identical patterns, with intensity and 2θ values plotted on the *Y*-axis and *X*-axis, respectively. The presence of characteristic peaks of pure ZnO-NPs was confirmed through the XRD diffractogram with 2θ values at 31.80° (1 0 0), 34.44° (0 0 2), 36.27° (1 0 1), 47.55° (1 0 2), 56.62° (1 1 0), 62.89° (1 0 3), 66.46° (2 0 0), 67.97° (1 1 2), and 69.05° (2 0 1), which were matched with the ICDD database card no. # 00-036-1451, indicating a hexagonal crystal structure with a face-centered lattice (space group 186: *P*63*mc*). The XRD patterns of the doped samples showed no additional diffraction peaks associated with Ag, Cu, Ca, Co, or Fe phases, indicating full metal ion incorporation into the ZnO lattice by substituting Zn^{2+} ions without altering the crystal structure because the doping levels were within the solubility limit.[35]

Based on the crystallographic diffractogram data, various crystal properties, including unit cell parameters, crystallite dimensions, microstrain, unit cell volume, dislocation density, and the specific surface area, were computed using equations given in the ESI† (eqn (S1)–(S6)) and data were arranged in Table 1.

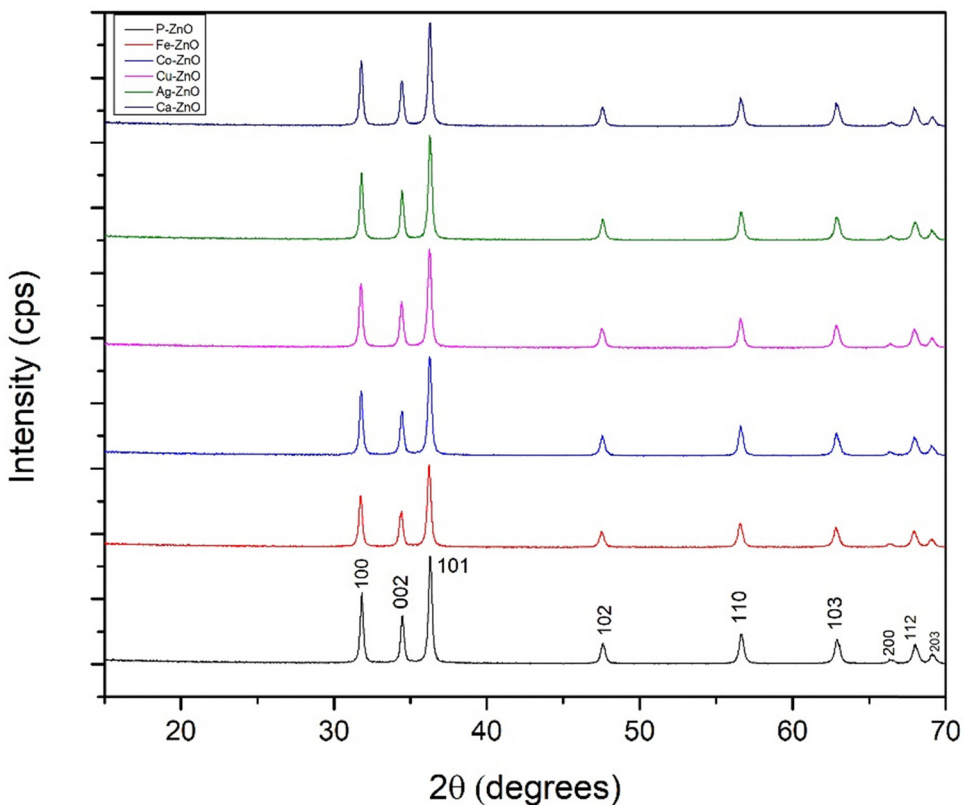

Fig. 2 X-ray diffractogram of pure and 0.5% Ag, Cu, Co, Fe, Ca doped ZnO-NPs.

Table 1 Parameters of chemically precipitated pure and doped ZnO nanoparticles based on XRD analysis

Parameter	PZO	AgZO	CuZO	CoZO	FeZO	CaZO
Lattice parameter, Å	In card no. # 00-036-1451: $a = b = 3.24982$ $c = 5.20661$					
	$a = b = 3.246$; $c = 5.2034$	$a = b = 3.251$; $c = 5.207$	$a = b = 3.251$; $c = 5.2094$	$a = b = 3.252$; $c = 5.2106$	$a = b = 3.254$; $c = 5.2142$	$a = b = 3.251$; $c = 5.208$
Macrostrain, ε	$\varepsilon = 15.32 \times 10^{-2}$	14.98×10^{-2}	15.70×10^{-2}	14.93×10^{-2}	16.17×10^{-2}	15.24×10^{-2}
Unit cell volume, Å^3	$V = 47.48$	47.65	47.68	47.72	47.81	47.67
Dislocation density (10^3 lines per m^2)	$\delta = 1.01$	0.972	1.065	0.962	1.122	1.007
Specific surface area, g^{-1} m^2	$S = 0.3404$	0.3340	0.3497	0.3322	0.3589	0.3401
Preference growth, PG	PG = 0.0072	0.0204	0.0086	0.012	0.0146	0.019

3.2. Crystal size estimation using different XRD models

3.2.1. Scherrer's model. A popular formula for determining the size of a nanoparticle's crystallite based on the widening of individual diffraction peaks is the Scherrer equation.[36] As per the Scherrer documentation, the formula for fine powder samples with cubic crystallites can be expressed as follows in eqn (3).

$$\text{Crystallite size, } D_{hkl} = \frac{K\lambda}{\beta_{hkl}\cos\theta} \quad (3)$$

The full width at half maximum (FWHM) of the *hkl* plane is indicated by β_{hkl} (in radians) in the formula above, while the wavelength of X-rays emitted from Cu (copper), 1.5406 Å, is represented by λ. In terms of the shape factor, the widely recognized Scherrer constant is 0.9.[37] According to the planes with the highest intensities, Table 2 shows the average crystallite sizes of pure and Ag, Cu, Co, Fe, and Ca doped ZnO.

3.2.2. Williamson–Hall model. The previously discussed approaches concentrated exclusively on peak widening caused by the crystallite particle size; however, other factors that can impact peak broadening and, in turn, particle size include boundaries, microstrain, crystal defects, and instrumental effects.[38,39] The fundamental idea behind this model is that it relies on the combined widening, which combines the effects of strain broadening (β_{strain}) and size broadening (β_{size}), with the total broadening being a combination of these two elements, which is shown in eqn (4).

$$\beta_{total} = \beta_{size} + \beta_{strain} \quad (4)$$

The uniform deformation model (UDM), uniform stress deformation model (USDM), and uniform deformation energy density model (UDEDM) are three modifications of the W–H model that have been used to calculate crystallite size, strain and stress.[40] Additionally, other models, such as Scherrer's model with a linear straight-line method, the Monshi–Scherrer method, Sahadat–Scherrer's model, and the size–strain plot, are explained in detail in Supplementary File S2 (ESI†).

The energy density, strain, and crystallite size of PZO and various metal doped ZnO-NP samples are revealed by the X-ray diffraction analysis. The smallest crystallite sizes ranging from 29.85 to 32.25 nm were obtained using Scherrer's equation and the Monshi–Scherrer approach estimates slightly bigger values of up to 38.79 nm. As LSLMSE accounts for each peak broadening and lattice distortions, it shows the largest sizes between 72.9 nm and 106.6 nm. The Williamson–Hall method is used to calculate the energy density (16.8–35.3 J m^{-3}), stress (976×10^5–122×10^6 N m^{-2}), strain (0.0007–0.0011), and intermediate diameters (41.98–55.43 nm). The size–strain approach provides the crystallite size between 32.99 nm and 43.3 nm. Overall, AgZO NPs exhibit relatively larger crystallite sizes with moderate strain, which may indicate structural changes caused by doping that enhance specific properties. The differences in crystallite sizes arise because each model considers different factors such as strain, defects, and peak broadening effects. While the Scherrer model assumes size-dependent broadening, models like Williamson–Hall and the strain–stress plot account for both crystallite size and microstrain, leading to variations in results.

3.3. Texture coefficient

In general terms, a plane's texture coefficient for a crystallite reflects its deviation from the reference sample, implying a

Table 2 Evaluation of ZnO-NPs' microstructural characteristics using various models

Model name		Crystal size (D, nm), energy density (u, J m^{-3}), stress (ε, N m^{-2})					
		P–ZO	Ag–ZO	Cu–ZO	Co–ZO	Fe–ZO	Ca–ZO
Scherrer's equation		$D_S = 31.48$	32.08	30.64	32.25	29.85	31.52
Williamson–Hall method	UDM	$\varepsilon = 0.0011$	$\varepsilon = 0.0009$	$\varepsilon = 0.0007$	$\varepsilon = 0.0009$	$\varepsilon = 0.0008$	$\varepsilon = 0.0009$
		$D_w = 55.43$	$D_w = 51.32$	$D_w = 41.99$	$D_w = 49.49$	$D_w = 41.98$	$D_w = 49.48$
	USDM	$\sigma = 1569 \times 10^5$	$\sigma = 1326 \times 10^5$	$\sigma = 976 \times 10^5$	$\sigma = 122 \times 10^6$	$\sigma = 1116 \times 10^6$	$\sigma = 1287 \times 10^5$
		$D_w = 55.43$	$D_w = 51.32$	$D_w = 41.99$	$D_w = 49.48$	$D_w = 41.99$	$D_w = 49.48$
	UDEDM	$u = 35.3$	$\sigma = 31.2$	$\sigma = 16.8$	$\sigma = 26.6$	$\sigma = 22.4$	$\sigma = 29.6$
		$D_w = 55.43$	$D_w = 51.32$	$D_w = 41.99$	$D_w = 49.48$	$D_w = 41.99$	$D_w = 49.48$
LSLMSE		$D_L = 106.6$	92.4	72.9	92.4	86.6	99
Monshi–Scherrer method		$D_M = 38.79$	32.43	35.01	38.36	34.5	37.53
Sahadat–Scherrer's model		$D_{(s-s)} = 32.22$	35.53	30.78	32.99	30.12	32.22
Size–strain plot		$D_w = 43.3$	32.99	37.44	40.75	36.46	41.98

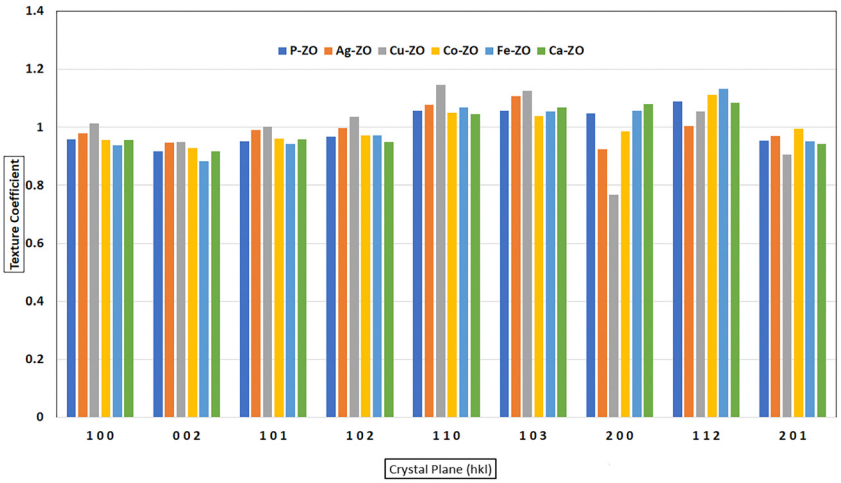

Fig. 3 Graphical representation of texture coefficients of synthesized pure and various metal doped ZnO-NPs.

directional preference in crystallite growth. The method described in eqn (5), which shows intensity peaks for the planes (100), (002), (101), (102), (110), (103), (200), (112), and (201), can be used to calculate the texture coefficient T_C based on an X-ray assessment.

$$\text{Texture coefficient, } T_{C_{(hkl)}} = \frac{I_{(hkl)} \Big/ I_{o_{(hkl)}}}{N^{-1}} \left(\sum I_{(hkl)} \Big/ I_{o_{(hkl)}} \right)^{-1} \quad (5)$$

The calculated values of the texture coefficient, with the corresponding graph, are illustrated in Fig. 3. The (110) and (103) planes show the highest texture coefficient values, suggesting that ZnO and its doped forms exhibit significant crystal growth along these orientations. The (100), (002), and (101) planes have relatively lower T_C values, implying that these orientations are less dominant. Some doped samples show slightly enhanced texture coefficients in specific orientations (AgZO and CuZO in the (110) and (103) planes).

3.4. Functional group analysis (FTIR)

The functional groups in synthesized nanoparticles were investigated using FTIR spectroscopy, as shown in Fig. 4a, which analyzed the absorption spectra of pure and doped ZnO-NPs of Ag, Cu, Co, Fe, and Ca in the wavelength range of 400 cm^{-1} to 4000 cm^{-1}. The region from 400 to 750 cm^{-1} is associated with the bonding between metal and oxygen atoms.[41] In terms of wavenumber per centimeter, the anticipated absorption maxima for ZnO nanoparticles are 2362, 1518, and 541.8 for vibrational modes of CO_2, bending vibration of H–O–H and stretching of Zn–O vibration, respectively.[42,43] Bond length changes brought about by the partial substitution of various metal dopant ions, such as Ag^+, Cu^{2+}, Co^{2+}, Fe^{3+}, and Ca^{2+}, for ZnO lattice sites may be correlated with shifts in the absorbance peak position shown in Fig. 4b. Additionally, the findings verify that the manufactured ZnO NP samples include no unnecessary components.

3.5. Morphology and EDAX analysis

Field emission scanning electron microscopy (FESEM) analysis was performed to study the surface morphology of chemically synthesized ZnO-NPs, both pure and doped, with the corresponding SEM images displayed in Fig. 5. Observations revealed that the ZnO-NPs had spherical grains, which were densely clustered and tightly grouped together due to agglomeration on the surface and the same data were observed in recent research.[31] High temperatures during the drying and calcination stages may lead to the clustering of ZnO particles. The particle size was analyzed, and the average sizes of pure ZnO and Ag-, Cu-, Co-, Fe-, and Ca-doped ZnO were found to be 107, 98, 93, 109, 102, and 129 nm, respectively, using ImageJ software.

The chemical composition of both pure and metal-doped ZnO-NPs was further examined using energy dispersive X-ray analysis (EDAX). It also revealed that pure ZnO-NPs had an elemental composition of 83.82% zinc (Zn) and 16.18% oxygen (O). The weight percentages of each doped metal with respect to Zn and O were as follows: 0.2% for Ag, 0.38% for Cu, 1.13% for Co, 0.36% for Fe, and 0.19% for Ca. Furthermore, it is evident from the study that none of the samples contain any contaminants.

3.6. HR-TEM analysis

High-resolution TEM is performed to support other analytical results and to analyze particle size and surface morphology with greater precision. In addition to spherical particles, hexagonal honeycomb structures are also visible, denoted by red arrows in Fig. 6(a). Using ImageJ software, the size of 25 individual particles was determined. The results showed an average of 92.18 nm and a size range of 28 to 130 nm (Fig. 6b),

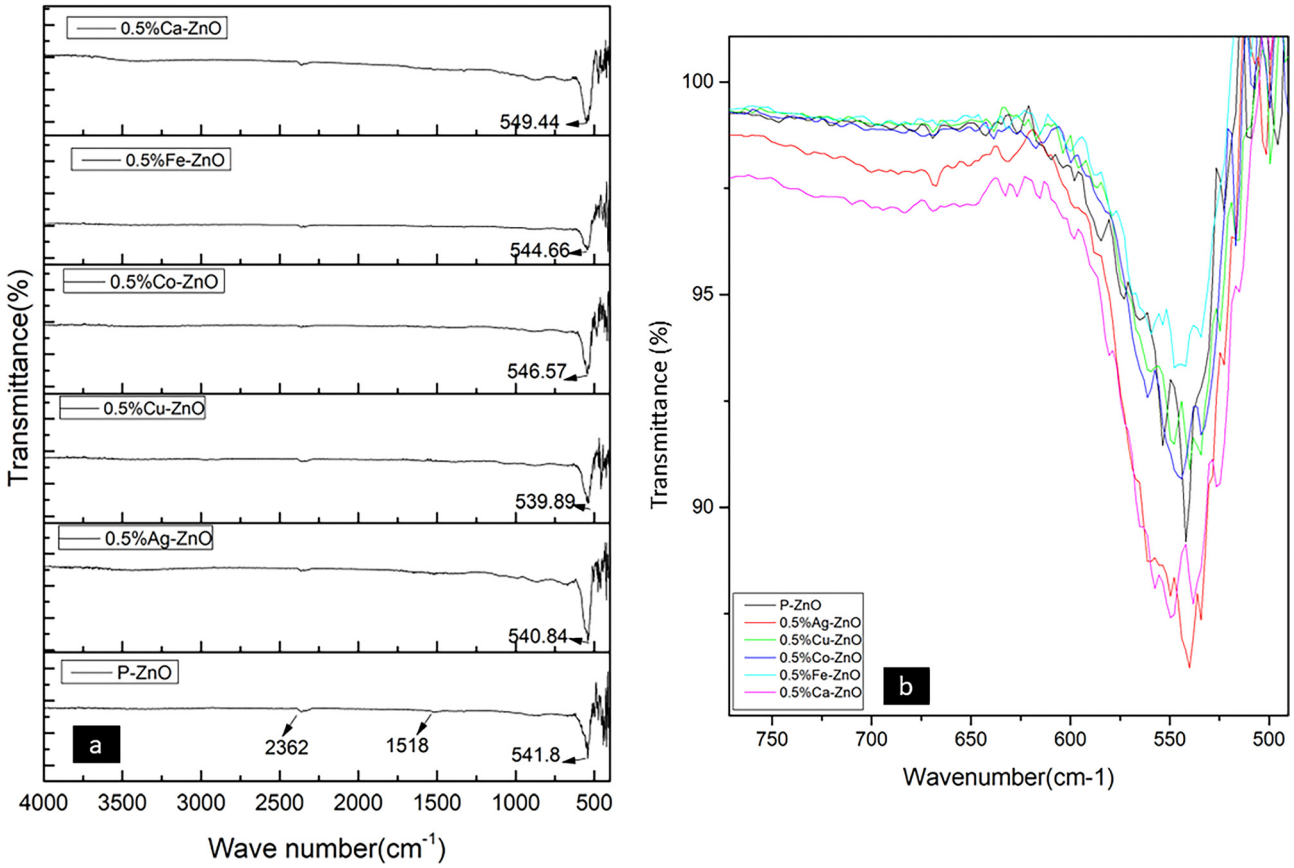

Fig. 4 (a) and (b) FTIR absorption spectra of various metal doped ZnO nanoparticles.

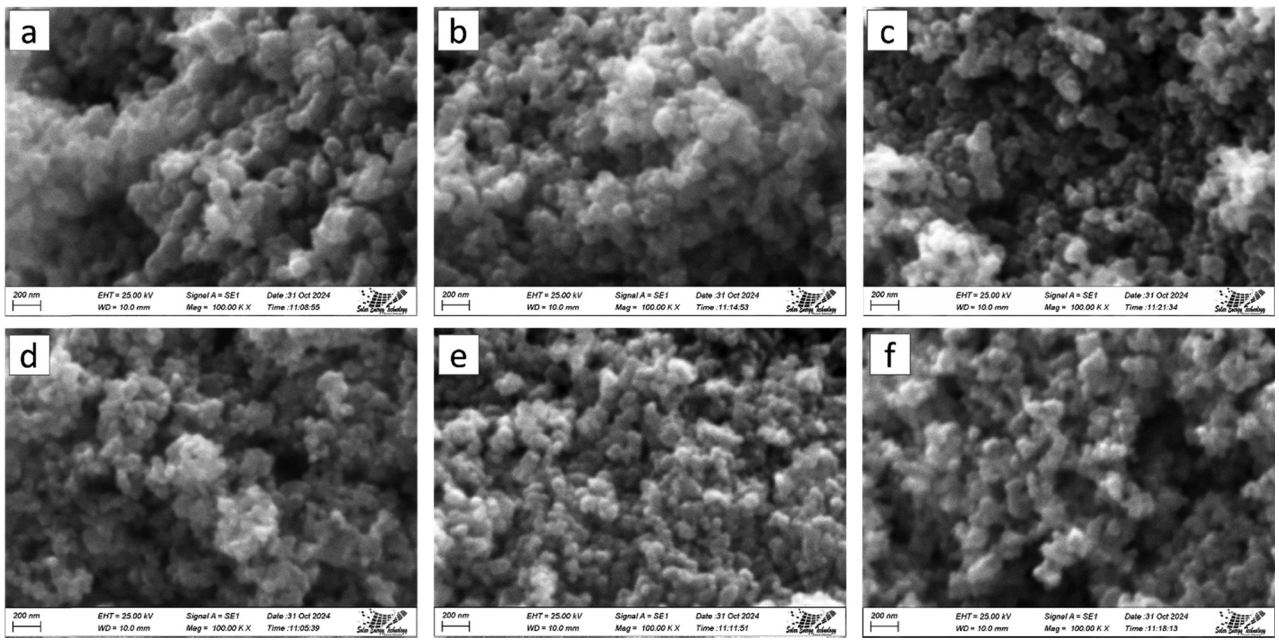

Fig. 5 FESEM images of (a) P–ZO, (b) Ag–ZO, (c) Cu–ZO, (d) Co–ZO, (e) Fe–ZO, and (f) Ca–ZO nanoparticles.

which is in line with previous SEM and XRD findings. The SAED pattern, which shows Debye–Scherrer rings corresponding to the planes (100), (102), (101), (102), (110), (103), (200), and (112), as shown in Fig. 6(c), validates the polycrystalline nature of the produced AgZO. Because of the higher molecular weight of Ag compared to Zn, dark patches within the ZnO-NPs indicate the presence of Ag ions. In accordance with findings from prior investigations, the interplanar spacing of AgZO, as

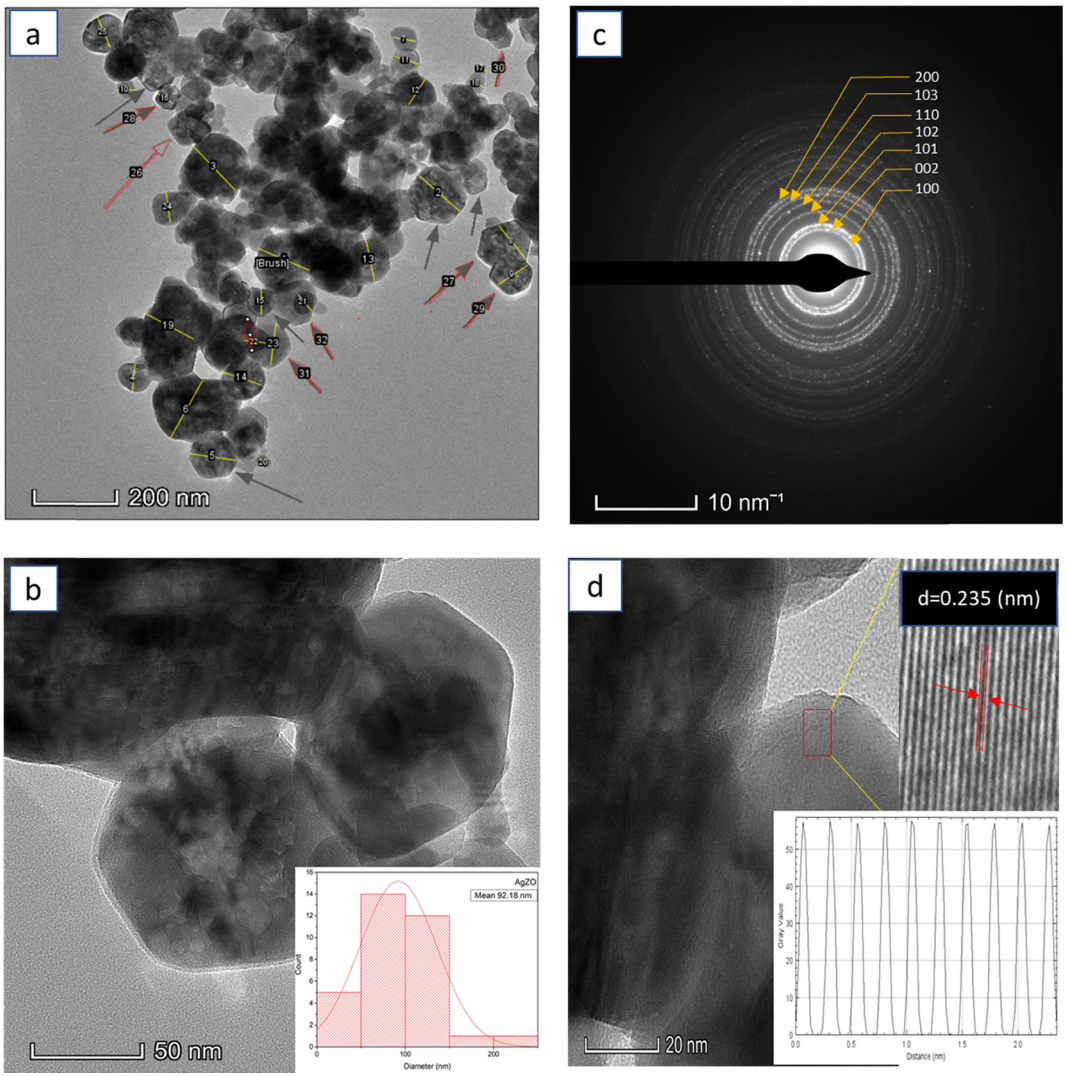

Fig. 6 HR-TEM images of AgZO NPs for analyzing (a) morphology and particle size, (b) particle size distribution histogram, (c) SAED pattern, and (d) interplanar spacing measurements.

measured by ImageJ software and displayed in Fig. 6(d), was 0.235 nm, for the (101) plane.[31]

3.7. Band gap analysis

The optical band gap energy is the smallest amount of energy required to excite an electron from the valence band to the conduction band, permitting optical absorption and electronic transitions. The band gap of both pure and Ag-doped ZnO-NPs was determined using UV-vis-NIR spectroscopy. The corresponding figure, which was obtained from Tauc's equation followed by the Kubelka–Munk equation in eqn (6), is displayed in Fig. 7.[44]

$$\alpha h\nu = A \times (h\nu - E_g)^2 \quad (6)$$

Here, α refers to the absorption coefficient, and A is a constant dependent on the material, whereas h denotes the photon energy and E_g signifies the optical band gap energy. Four distinct types of band transitions were identified, with an exponent of 1/2 indicating direct allowed transitions, while 3/2, 2, and 3 correspond to direct forbidden, indirect allowed, and indirect forbidden transitions, respectively.[45] In the case of ZnO-NPs, a direct allowed transition occurs, with the band gap energy measured at 3.16 eV for pure ZnO. After doping with Ag ions, the band gap remains nearly the same at 3.168 eV in this study. Almost similar results have been documented in previous research on AgZO.[46]

3.8. TGA analysis

Thermogravimetric analysis (TGA) was used to assess the thermal stability of pure and Ag-doped ZnO-NPs, calcined at 500 °C, by measuring the weight loss. As depicted in Fig. 8, about 2% of the moisture content is removed between 50 and 7000 °C, while the PZO sample demonstrates nearly 5% weight loss. Both samples exhibit a rapid weight reduction in the range of 50–150 °C, with the weight loss of PZO being higher than that of pure ZnO due to the physically adsorbed surface water

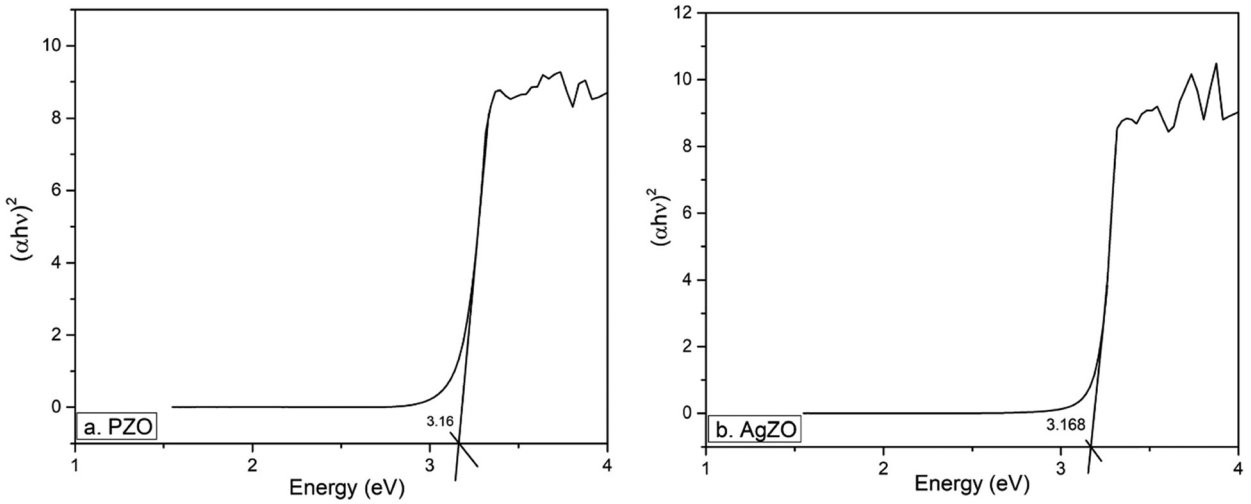

Fig. 7 Optical band gap estimation of (a) PZO and (b) AgZO nanoparticles.

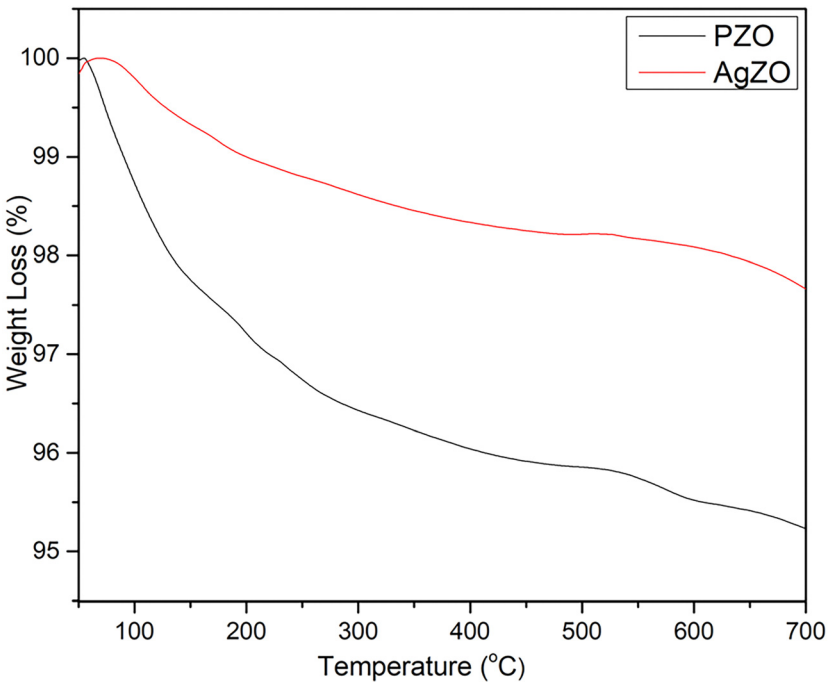

Fig. 8 TGA curves of PZO and AgZO nanoparticles.

content. A minor weight loss observed between 150 and 400 °C is likely due to the release of chemically adsorbed water.[47] At temperatures above 500 °C, the amorphous phase transforms into a crystalline structure, during which the remaining water is expected to evaporate, leading to a decrease in weight. Since the samples were previously calcined, this indicates that pure ZnO-NPs adsorbed more moisture compared to Ag-doped ZnO-NPs.

3.9. Particle size analysis

Using the dynamic light scattering (DLS) method, the particle size of the synthesized products was determined; the results are shown in Fig. 9. The samples were dispersed in water and sonicated for 10 minutes to achieve a uniform dispersion, ensuring suitability for DLS measurements. This technique determines the particle size of the sample by measuring its hydrodynamic volume, based on the Brownian motion of the particles.[48] The hydrodynamic volumes of PZO and AgZO were found to average 293 nm and 383 nm, respectively, which were significantly larger than the theoretical sizes previously determined using FESEM and TEM.

3.10. Photocatalytic activity evaluation

The synthesized ZnO-NPs, available in pure form or doped with metals like Ag, Cu, Co, Fe, or Ca, act as powerful photocatalysts

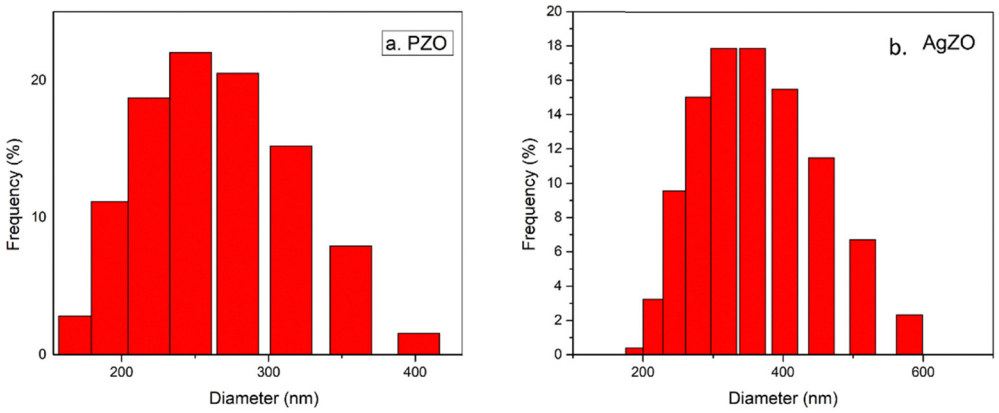

Fig. 9 The DLS method was utilized to analyze the particle sizes of (a) PZO and (b) AgZO samples.

for degrading textile dyes such as Congo Red (CR). Under visible light irradiation, the photocatalytic activity of the generated ZnO-NPs with time is shown in Fig. 10. This study evaluated the rate of degradation and capacity of 0.075 g of both pure and doped ZnO-NPs over 30, 60, 90, and 120-minute intervals, employing UV-visible spectrum analysis for measurement. Both curves, a and b, indicate that the degradation percentage and capacity increased over time. The study found that although Fe–ZO initially exhibited a higher degradation rate, Cu–ZO, Ag–ZO and PZO ultimately achieved the highest degradation levels, reaching 95.17%, 94.81% and 94.81%, with degradation capacities of 5.02, 4.99 and 4.99, respectively, after 180 minutes of irradiation under visible light. However, Fe–ZO, Ca–ZO, and Co–ZO likewise demonstrated notable degradation abilities of 94.27, 94.09, and 93.92%, with the corresponding degradation capacities of 4.96, 4.95, and 4.94. The comparison study with other recent research studies is displayed in Table 3.

3.11. Scavenger test

Scavengers are substances added to a reaction during chemical treatment in order to either remove or deactivate undesirable products. Degradation of persistent organic pollutants in water is mostly dependent on reactive oxygen species (ROS), which are produced during visible light-induced photocatalysis and include free radicals such as hydroxyl groups ($^{\bullet}OH$), and pair of electron–hole and hydrogen peroxide (H_2O_2). The involvement of various ions and radicals in dye breakdown was examined through a scavenger test. The specific roles of destructive agents, including $^{\bullet}O^{2-}$, H^{+}, and $^{\bullet}OH$, were identified using inhibitors like DPPH, EDTA, and IPA.[60] In this research, the functions of free radicals and hydroxyl groups in CR degradation were

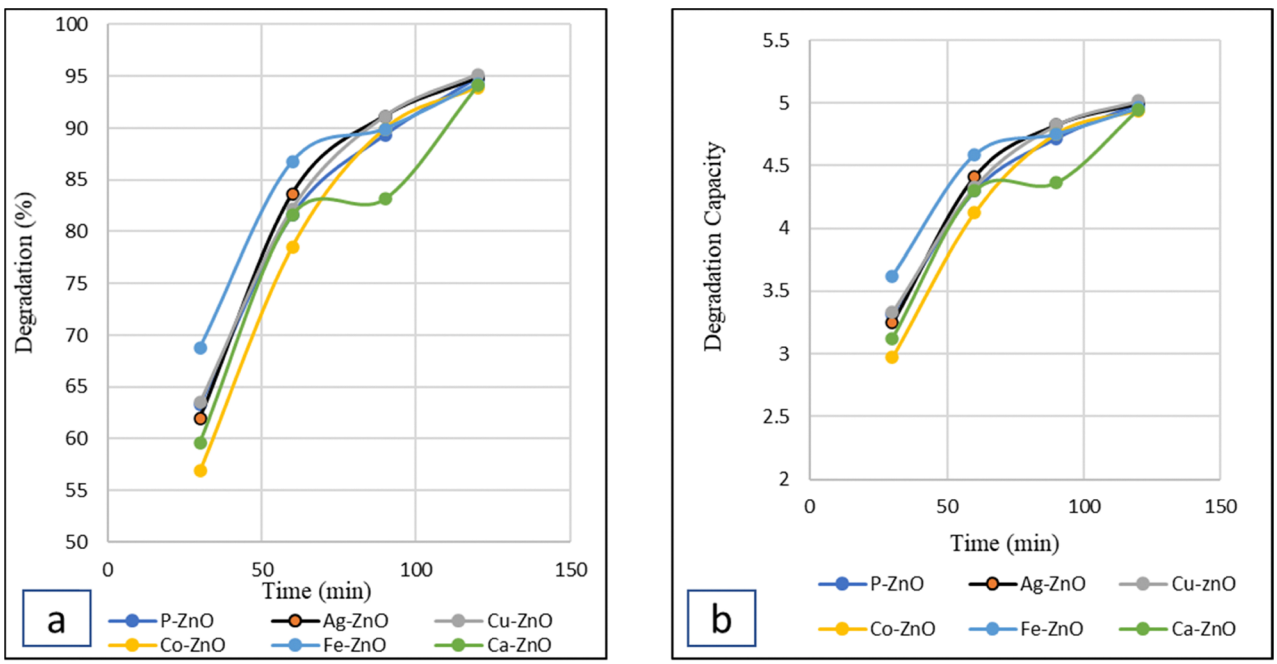

Fig. 10 Photocatalytic degradation (a) and degradation capacity (b) curve of CR dye with pure and several metal-doped ZnO nanoparticles.

Table 3 Comparative study of the photocatalytic degradation performance of pure and various metal doped ZnO nanoparticles

Sample; amount (mg)	Dye	Time	Degradation (%)	Ref.
Ag–ZnO; 0.1	CR	120 min under UV	60.5	49
Ag–ZnO	CR		86	50
Fe–ZnO; 300 mg L^{-1}	MB	60 min under visible light	94.21	51
	CR		32.97	
C–ZnO; 0.1	RhB	240 min under UV	99	29
Co–ZnO; 0.025	CR	60 min under a xenon lamp	90.12	52
ZnO (olive fruit); 30 mg	MB	180 min under sunlight exposure	75	53
	MO		87	
ZnO (*Equisetum diffusum*)	MB	120 min under sunlight exposure	85.61	54
	MO		79.10	
ZnO (*C. macrocarpa*)	MB	120 min under sunlight exposure	82.2	55
	MO		87.5	
Mg–ZnO; 0.05	RhB	120 min under UV	78	56
Cu–ZnO; 120 mg L^{-1}	CR	140 min under UV	97	57
Mn–ZnO; 0.15	CR	180 min under UV	92	58
Cr–ZnO; 0.05	CR	60 min under visible light	94	59
PZO	CR	120 min under visible light	94.81	This work
AgZO			94.81	
CuZO			95.17	
CoZO			93.92	
FeZO			94.28	
CaZO			94.2	

analyzed using DPPH and IPA solutions. A mixture of 10 mL of DPPH (8 ppm), 10 mL of IPA (0.1 M), 0.075 g of the sample, and 40 mL of deionized water was prepared in a beaker for the experiment. A beaker was prepared containing 40 mL of dye solution with 0.07 g of each sample and then 10 mL of DPPH (8 ppm) and 10 mL of IPA (0.1 M) solution were added to each beaker. A beaker containing 40 mL of dye solution and 0.07 g of the sample was set up under a visible lamp for 120 minutes, with 10 mL of DPPH (8 ppm) and 10 mL of IPA (0.1 M) solutions added separately. As depicted in Fig. 11, degradation diminished for all samples upon the addition of DPPH and IPA solutions, with the values falling within 39–73% and 45–56%, respectively. Since the addition of IPA results in a more noticeable decrease in efficiency, the data indicate that hydroxyl radicals are the main source of deterioration.

3.12. Recyclability and stability of the sample

A recyclability assessment was conducted to evaluate the durability of the synthesized catalyst by analyzing its effectiveness in degrading the CR dye. To investigate the catalyst's reusability for CR dye degradation, a 40 mL dye solution (10 ppm) was mixed with 0.07 g of the catalyst in a beaker and subjected to halogen lamp illumination for 120 minutes. The procedure involved conducting three cycles, during which the catalyst underwent a washing and decanting process three times using water after the completion of each cycle. Subsequently, the catalyst was dried in an oven at 80 °C before being utilized in the next cycle. As illustrated in Fig. 12, the percentage of degradation exhibited a gradual decrease. The total degradation efficiency reduced from a peak value of 95% for CuZO to 61% for PZO. The decline in photocatalytic efficiency observed for both pure and doped ZnO catalysts can be attributed to two primary factors. Firstly, repeated usage leads to surface blockage, thereby hindering catalytic activity. Secondly, catalyst leaching occurs during the washing and separation processes, further contributing to efficiency reduction.[61]

3.13. Kinetics of photodegradation

The widely recognized Langmuir–Hinshelwood model equation was employed to determine the rate of dye degradation. This model

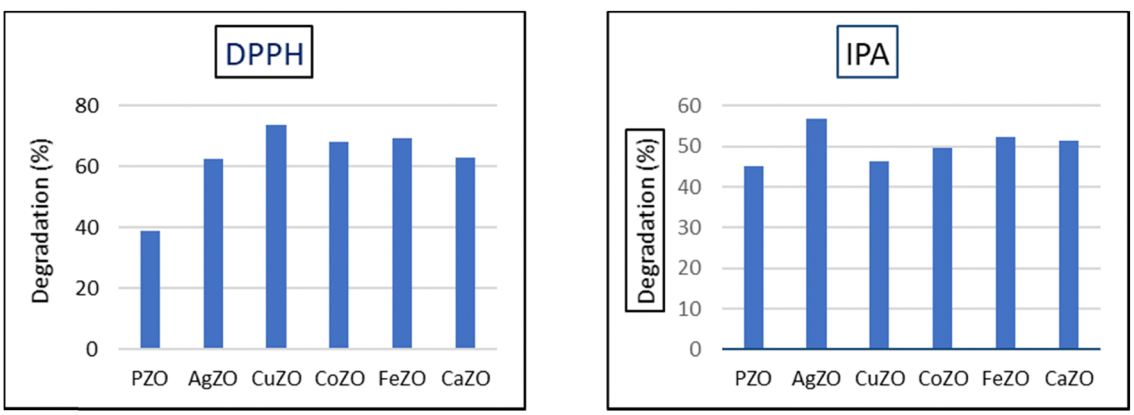

Fig. 11 Free radical and hydroxyl scavenging test with DPPH and IPA solutions for pure and doped ZnO-NPs.

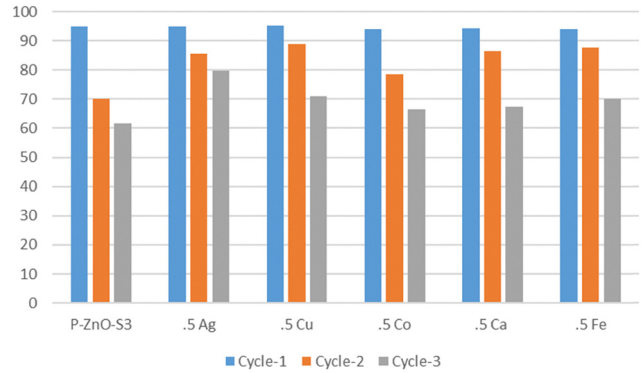

Fig. 12 Reusability test of pure and doped ZnO NPs.

establishes a mathematical relationship, expressed in eqn (7), that describes how the concentration varies over time (t, in minutes) in relation to the degradation rate.[62]

$$r = -\frac{dc}{dt} = \frac{k_r k_{ae}}{1 + k_{ae} C} \quad (7)$$

Here, r is the rate of the reaction and k_r and k_{ae} are the rate constant and adsorption constant respectively. Eliminating the denominator and treating C_0 at t = 0 as negligible due to its relatively low value, eqn (8) is reformulated as follows[63]

$$-\ln\left(\frac{C_t}{C_0}\right) = k_r k_{ae} t = K_{app} t \quad (8)$$

The calculated slope from the plotted graph corresponds to the observed first-order rate constant (K_{app}). Analysis of the six samples revealed a consistent linear trend, implying that the photodegradation process proceeded according to first-order reaction kinetics. According to the data depicted in Fig. 13, the rate constants estimated from the graph correspond to 0.019 min^{-1} for pure, 0.0207 min^{-1} for CuZO, 0.02 min^{-1} for both AgZO and CoZO, 0.016 min^{-1} for CaZO, and 0.017 min^{-1} for FeZO. The photodegradation rate constants of ZnO nanoparticles synthesized *via* a recent green method were determined to be 0.008 min^{-1} for MB and 0.013 min^{-1} for MO.[53] Similarly, gold nanoparticles produced through a green synthesis approach exhibited a photodegradation rate constant of 0.0791 min^{-1} for MB degradation.[64] Additionally, another study reported rate constants of 0.022 min^{-1} and 0.025 min^{-1} for the degradation of MO and MB, respectively, at 90 °C.[55]

3.14. Antimicrobial activity evaluation

The six samples showed antibacterial activity against all tested Gram-positive bacteria such as *B. cereus*, *L. monocytogenes*, *monocytogenes* and *S. aureus* and in the case of Gram-negative bacteria *E. coli*, only the AgZO sample showed a clear zone of inhibition (20.8 mm) in agar diffusion assay shown in Table 4 and Fig. 14. Against *S. aureus*, the activity levels of all samples are nearly identical, whereas PZO exhibits a remarkable activity against *L. monocytogenes* with the lowest MBC (0.625 mg mL^{-1}) and MIC (0.313 mg mL^{-1}) values. Among the six samples, AgZO showed antibacterial activity against all tested bacteria and between 1.25 and 5 mg mL^{-1} concentration, the sample was able to kill 99.9% bacterial population after 24 h of incubation under shaking conditions (Table 5 and Fig. 15). The precipitation rate of ZnO-NPs is higher than the diffusion rate in agar media and this could be a possible reason that in well diffusion

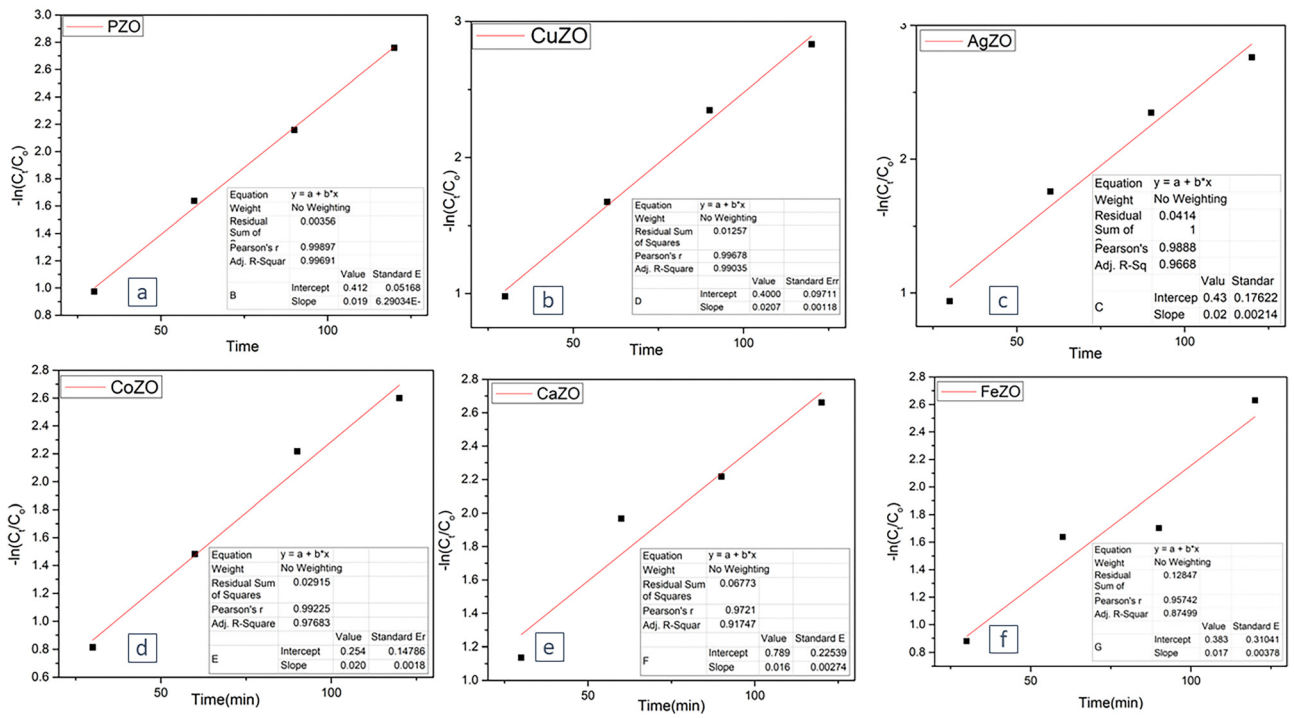

Fig. 13 A first-order kinetics approach was employed to interpret the experimental results concerning the photocatalytic degradation of the CR dye.

Table 4 Antibacterial activity of pure and doped ZnO-NPs

Names of tested microorganisms				
	Gram-positive		Gram-negative	
Sample name	*S. aureus*	*L. monocytogenes*	*B. cereus*	*E. coli*
	Diameter of zone of inhibition (mm)			
P–ZO	10.17 ± 0.29	12.2 ± 1.04	11.7 ± 0.76	<6
Ag–ZO	10.2 ± 0.35	11.2 ± 0.29	10.2 ± 0.29	20.8 ± 0.80
Cu–ZO	10.3 ± 0.81	13.3 ± 1.53	11.0 ± 0.50	<6
Co–ZO	10.0 ± 0.93	10.5 ± 0.50	13.5 ± 1.32	<6
Fe–ZO	10.5 ± 0.50	12.2 ± 0.29	10.5 ± 0.50	<6
Ca–Zo	10.1 ± 0.45	13.2 ± 0.29	10.7 ± 0.29	<6
Positive control	15.7 ± 0.76	16.8 ± 1.61	14.8 ± 1.61	20.7 ± 0.76

* <6 mm = no significant antibacterial activity was observed.

Table 5 Minimum inhibitory concentration (MIC) and minimum bactericidal concentration (MBC) of ZnO-NPs

	B. cereus		*L. monocytogenes*		*S. aureus*		*E. coli*	
	MIC	MBC	MIC	MBC	MIC	MBC	MIC	MBC
Sample name	Concentration, mg mL^{-1}							
P–ZO	5	10	0.313	0.625	5	5	—	—
Ag–ZO	1.25	2.5	0.625	1.25	5	5	1.25	2.5
Cu–ZO	5	10	0.625	1.25	5	5	—	—
Co–ZO	2.5	5	0.625	1.25	5	10	—	—
Fe–ZO	2.5	5	1.25	1.25	2.5	5	—	—
Cu–ZO	5	10	0.625	1.25	5	5	—	—

assay, the highest concentration (40 mg mL^{-1}) of samples was not able to form a clear zone of inhibition compared to the bactericidal activity (99.9% kill) shown by the samples at comparatively lower concentration (1.25–10 mg mL^{-1}) in MBC assay.

4. Environmental impact

While metal-doped ZnO nanoparticles, particularly those doped with Ag, Cu, Fe, and Ca, have shown remarkable efficacy in dye degradation and antimicrobial activity, their potential environmental impact remains a growing concern. The accumulation of ZnO-NPs in ecological systems may lead to their dissociation into zinc ions, potentially disrupting microbial communities by degrading beneficial or non-target microorganisms.[65] Since ZnO NPs are safe and non-toxic and contain only a minimal amount of metal, they cannot be classified as a highly toxic material.[13] Furthermore, as these nanoparticles are intended for reuse and will be recollected, there is no risk of their accumulation in the environmental cycle. Due to its insolubility in water, sophisticated filtration techniques may help prevent leaching. Future studies should focus on creating eco-friendly ways to make these nanoparticles, designing them to be safer, and finding effective ways to recover or collect them after use to avoid harming the environment.

5. Discussion

ZnO-NPs, being non-toxic, safe, and versatile, find applications across various fields, including dentistry,[66] toothpaste,[67] cosmetics,[68] and skin creams.[69] In addition to water treatment, ZnO-NPs are used as an effective bactericidal agent in these industries. To enhance the efficiency of ZnO-NPs in combating microorganisms and degrading dyes, various metal-doped ZnO-NP samples were synthesized. The efficacy of the ZnO-NPs has been significantly improved in recent studies through the doping of metals like silver, copper, iron, and cobalt, which effectively alter structural and crystallographic parameters.[70–73] In the present study, AgZO samples

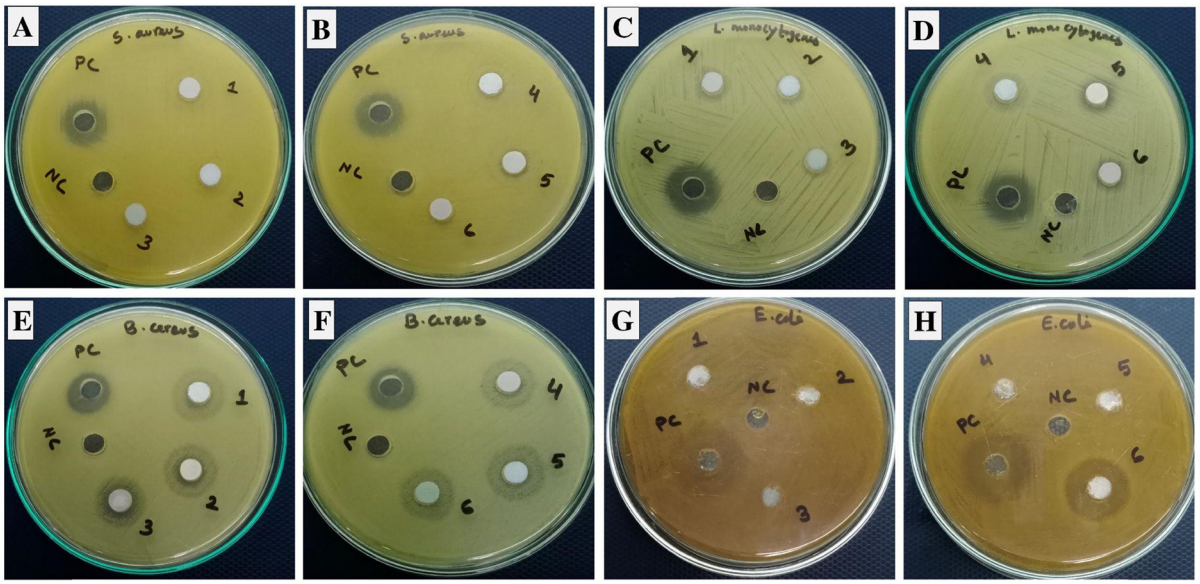

Fig. 14 Antibacterial activity of ZnO-NPs against (A) and (B) *S. aureus*; (C) and (D) *Listeria monocytogenes*; (E) and (F) *B. cereus*; and (G) and (H) *E. coli*. Here, 1 = Cu–ZO, 2 = P–ZO, 3 = Co–ZO, 4 = Ca–ZO, 5 = Fe–ZO, 6 = Ag–ZO. *PC = chloramphenicol 100 ppm; NC = distilled water (with 2% Tween 20).

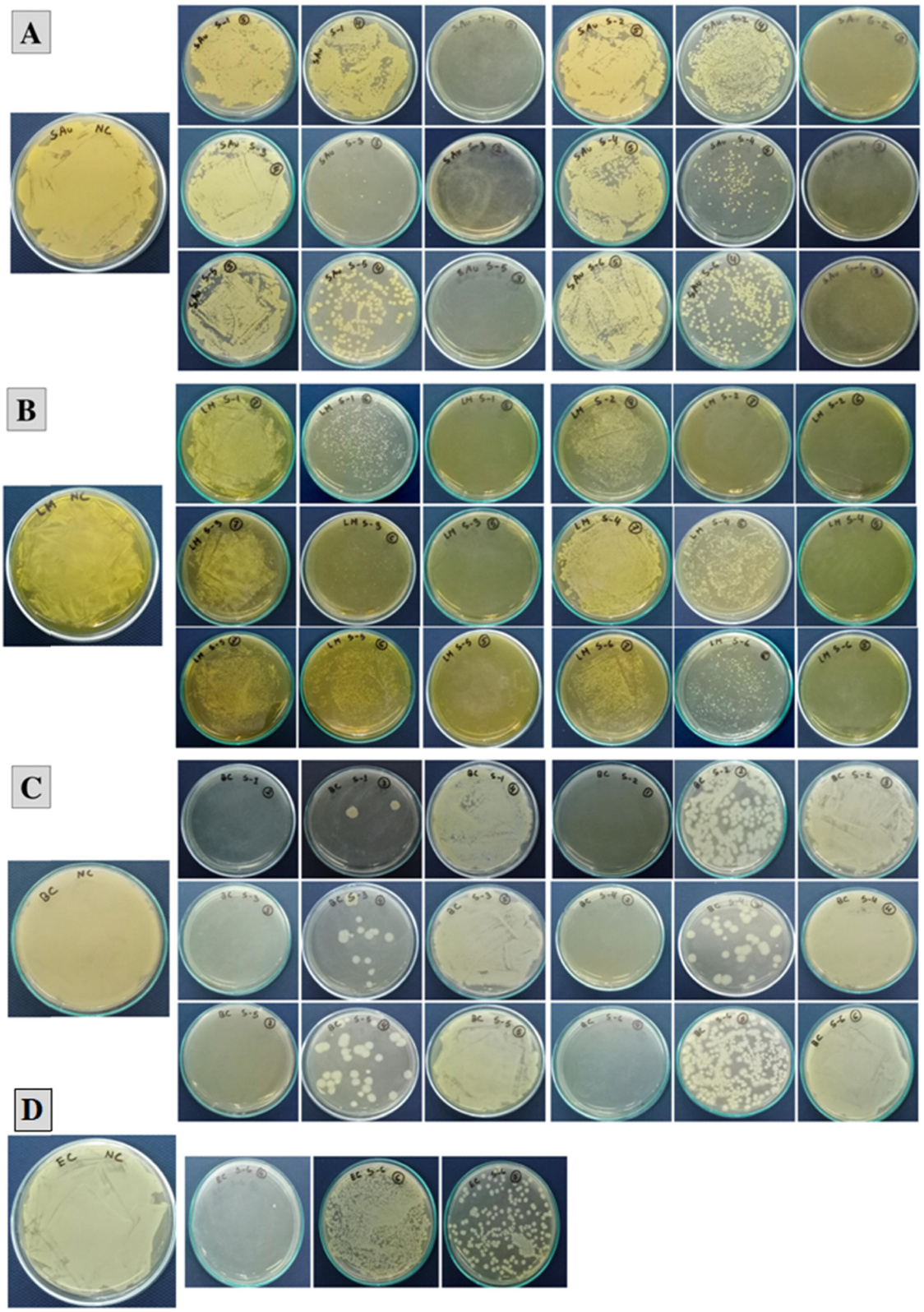

Fig. 15 Minimum bactericidal activity of ZnO-NPs, S-1 = Cu–ZO, S-2 = P–ZO, S-3 = Co–ZO, S-4 = Ca–ZO, S-5 = Fe–ZO, S-6 = Ag–ZO, against (A) *S. aureus*; (B) *Listeria monocytogenes*; (C) *B. cereus*; and (D) *E. coli*. The concentration of samples is diluted by a 2-fold serial dilution method, where, 1 = 20 mg mL^{-1}, 2 = 10 mg mL^{-1}, 3 = 5 mg mL^{-1}, 4 = 2.5 mg mL^{-1}, 5 = 1.25 mg mL^{-1}, 6 = 0.625 mg mL^{-1}, 7 = 0.313 mg mL^{-1}, and 8 = 0.157 mg mL^{-1}.

demonstrated heightened antimicrobial efficacy, eradicating 99.9% of Gram-positive and Gram-negative bacteria at concentrations of 1.25–5 mg mL^{-1}.

The synthesized PZO, with a band gap energy of 3.16 eV and nanoscale particle size, demonstrates enhanced photocatalytic and antimicrobial performance, achieving 94.81% degradation and inhibition zones of 10.17 ± 0.29 mm, 12.2 ± 1.04 mm, and 11.7 ± 0.76 mm against Gram-positive strains *S. aureus*, *L. monocytogenes*, and *B. cereus*, respectively, while showing no activity against Gram-negative *E. coli*. However. doping ZnO with Ag ions has mitigated this issue by amplifying the synergistic generation of ROS in both light and dark environments, facilitating the release of Ag^+ and Zn^+ ions,[74] possibly lowering the Fermi energy to enable electron migration from ZnO to Ag[75] and utilizing surface defects like oxygen vacancies to drive free radical formation.[76] Since Zn^{2+} and Ag^+ ions are nanometer-sized, much smaller than bacteria, they can penetrate the cell membrane and interact with negatively charged proteins and DNA, disrupting their function and ultimately killing the cell. Congo Red (CR) was photocatalytically broken down under a 500 W halogen lamp that was positioned 65 cm away from the sample. Owing to the nearly equivalent band gaps of PZO and AgZO, their degradation levels were close, with CuZO, AgZO, and PZO showing slightly higher values at 95.17%, 94.81%, and 94.81%, respectively. The photocatalytic degradation performance of FeZO, CaZO, and CoZO remains noteworthy, though marginally inferior to that of PZO, AgZO, and CuZO. The primary reason for this reduction in activity lies in their comparatively larger particle sizes, which obstruct active sites and diminish the formation of reactive oxygen species. Furthermore, texture coefficient values indicate that AgZO and CuZO exhibit the highest preferential growth along the 110 and 103 crystal planes, which may contribute to their superior catalytic efficiency compared to other doped variants. Through scavenger studies with DPPH and IPA, the role of reactive oxygen species (ROS), such as O^{2-}, H^+, and OH^-, in degrading dyes was evaluated. As can be shown in Fig. 7, which displays a decrease in degradation performance, these substances inhibit ROS activity.

In the future, additional research could focus on degrading emerging multidrug-resistant bacterial strains, as well as incorporating the material into various products to improve their usability and stability.

6. Conclusion

In this work, we have synthesized pure and various metal doped ZnO-NPs such as Ag, Cu, Co, Fe, and Ca ZnO-NPs through the cost effective and easy to operate chemical precipitation method, which show excellent photocatalytic dye degradation and antimicrobial activity. All synthesized samples, as confirmed by the XRD data, exhibited a wurtzite crystal structure and displayed a combination of spherical and hexagonal morphologies. Techniques like FESEM and HR-TEM are employed to measure particle sizes, which are found to range from 92.18 nm to 129 nm on average. Thermogravimetric analysis (TGA) shows the stability of PZO and AgZO up to 700 °C, with slight weight loss attributed to regained moisture. The optical band gap analysis supports the photocatalytic efficiency of PZO and AgZO nanoparticles, as their values are nearly identical at 3.16 eV and 3.168 eV. While no other samples exhibit effective activity against the Gram-negative bacterium *E. coli*, Ag-doped ZnO (AgZO) nanoparticles exhibit enhanced antibacterial effects on both Gram-positive and Gram-negative bacteria, producing inhibition zones of 12.2 ± 1.04 mm and 20.8 ± 0.80 mm, respectively, when compared to pure ZnO. However, all the samples demonstrate outstanding photocatalytic performance in degrading the Congo Red (CR) dye under simulated sunlight, with CuZO, AgZO and PZO achieving remarkable degradation efficiencies of 95.17%, 94.81%, and 94.81%, respectively.

Author contributions

Md. Atikur Rahman prepared and analyzed pure and doped ZnO, conducted the experiment, and wrote the draft and original manuscript. Md. Sahadat Hossain conceived and designed the experiment and analyzed the data. Md. Tanvir Hossain and Samina Ahmed supervised the findings of this work. Muhammad Shahriar Bashar and Md Farid Ahmed helped in data curation. Subarna Sandhani Dey performed a formal analysis. Samina Ahmed supervised the overall work and managed the required facilities.

Data availability

Data will be made available upon request from authors.

Conflicts of interest

There are no conflicts to declare.

Acknowledgements

The authors are grateful to the Bangladesh Council of Scientific and Industrial Research (BCSIR) authority for financial support through the R&D project (ref. no. 39.02.0000.011.14.134.2021/900; Date: 30.12.2021). Priya Paul thanks the Department of Applied Chemistry and Chemical Engineering, Noakhali Science and Technology University, Noakhali, Bangladesh, for approving the MS Thesis program.

References

1 Z. Ma, C. Liu, C. Srinivasakannan, L. Li and Y. Wang, Synthesis of Magnetic Fe_3O_4-HKUST-1 Nanocomposites for Azo Dye Adsorption, *Arab. J. Chem.*, 2023, **16**(6), 104767, DOI: 10.1016/j.arabjc.2023.104767.
2 B. Lellis, C. Z. Fávaro-Polonio, J. A. Pamphile and J. C. Polonio, Effects of Textile Dyes on Health and the

Environment and Bioremediation Potential of Living Organisms, *Biotechnol. Res. Innov.*, 2019, **3**(2), 275–290, DOI: 10.1016/j.biori.2019.09.001.

3 S. I. Siddiqui, E. S. Allehyani, S. A. Al-Harbi, Z. Hasan, M. A. Abomuti, H. K. Rajor and S. Oh, Investigation of Congo Red Toxicity towards Different Living Organisms: A Review, *Processes*, 2023, **11**(3), 807, DOI: 10.3390/pr11030807.

4 M. A. Salam, M. Y. Al-Amin, M. T. Salam, J. S. Pawar, N. Akhter, A. A. Rabaan and M. A. A. Alqumber, Antimicrobial Resistance: A Growing Serious Threat for Global Public Health, *Healthcare*, 2023, **11**(13), 1946, DOI: 10.3390/healthcare11131946.

5 D. E. Bloom and D. Cadarette, Infectious Disease Threats in the Twenty-First Century: Strengthening the Global Response, *Front. Immunol.*, 2019, 10, DOI: 10.3389/fimmu.2019.00549.

6 M. Shnayerson and M. J. Plotkin, *The Killers Within: The Deadly Rise Of Drug-Resistant Bacteria*, Reprint edition, Back Bay Books, 2003.

7 S. K. Ahmed, S. Hussein, K. Qurbani, R. H. Ibrahim, A. Fareeq, K. A. Mahmood and M. G. Mohamed, Antimicrobial Resistance: Impacts, Challenges, and Future Prospects, *J. Med. Surg. Public Health*, 2024, **2**, 100081, DOI: 10.1016/j.glmedi.2024.100081.

8 A. Muhammed, T. G. Asere and T. F. Diriba, Photocatalytic and Antimicrobial Properties of ZnO and Mg-Doped ZnO Nanoparticles Synthesized Using Lupinus Albus Leaf Extract, *ACS Omega*, 2024, **9**(2), 2480–2490, DOI: 10.1021/acsomega.3c07093.

9 M. J. F. Anik, S. R. Mim, S. S. Swapno, S. Munira, O. Roy and M. M. Billah, Vacancy Induced Enhanced Photocatalytic Activity of Nitrogen Doped CuO NPs Synthesized by Co-Precipitation Method, *Heliyon*, 2024, **10**(6), e27613, DOI: 10.1016/j.heliyon.2024.e27613.

10 M. Shabaninia, M. Khorasani and S. Baniyaghoob, Synthesis of Silver-Doped Titanium Dioxide Nanoparticles by Sol-Gel and Coprecipitation Techniques: Evaluation of Antimicrobial Activity and Cytotoxic Effects, *ChemistrySelect*, 2024, **9**(14), e202303358, DOI: 10.1002/slct.202303358.

11 A. Halfadji, L. Bennabi, S. Giannakis, A. G. Marrani and S. Bellucci, Sono-Synthesis and Characterization of next-Generation Antimicrobial ZnO/TiO_2 and Fe_3O_4/TiO_2 Bi-Nanocomposites, for Antibacterial and Antifungal Applications, *Ceram. Int.*, 2024, **50**(20, Part B), 39097–39108, DOI: 10.1016/j.ceramint.2024.07.276.

12 A. Verma, G. Sharma, T. Wang, A. Kumar, P. Dhiman and A. García-Peñas, Graphitic Carbon Nitride (g-C3N4)-Based Magnetic Photocatalysts for Removal of Antibiotics, *Carbon Lett.*, 2025, **35**, 45–73, DOI: 10.1007/s42823-024-00811-4.

13 A. T. Reda, J. Y. Park and Y. T. Park, Zinc Oxide-Based Nanomaterials for Microbiostatic Activities: A Review, *J. Funct. Biomater.*, 2024, **15**(4), 103, DOI: 10.3390/jfb15040103.

14 A. Abbas, S. Mansoor, M. H. Nawaz, A. A. Chaudhry, K. Ijaz, S. Riaz and A. Hayat, Growth of Diazonium-Functionalized ZnO Nanoflakes on Flexible Carbon Cloth for Electrochemical Sensing of Acetone in the Liquid Phase, *RSC Adv.*, 2023, **13**(17), 11537–11545, DOI: 10.1039/D3RA01268A.

15 S. Ullah, M. Shaban, A. B. Siddique, A. Zulfiqar, N. S. Lali, M. Naeem-ul-Hassan, M. I. Irfan, M. Sher, M. Fayyaz ur Rehman, A. Hanbashi, F. Y. Sabei, H. M. A. Amin and A. Abbas, Greenly Synthesized Zinc Oxide Nanoparticles: An Efficient, Cost-Effective Catalyst for Dehydrogenation of Formic Acid and with Improved Antioxidant and Phyto-Toxic Properties, *J. Environ. Chem. Eng.*, 2024, **12**(5), 113350, DOI: 10.1016/j.jece.2024.113350.

16 K. M. Lee, C. W. Lai, K. S. Ngai and J. C. Juan, Recent Developments of Zinc Oxide Based Photocatalyst in Water Treatment Technology: A Review, *Water Res.*, 2016, **88**, 428–448, DOI: 10.1016/j.watres.2015.09.045.

17 M. Ahmad, J. Zhao, J. Iqbal, W. Miao, L. Xie, R. Mo and J. Zhu, Conductivity Enhancement by Slight Indium Doping in ZnO Nanowires for Optoelectronic Applications, *J. Phys. Appl. Phys.*, 2009, **42**(16), 165406, DOI: 10.1088/0022-3727/42/16/165406.

18 A. N. Tuama, L. H. Alzubaidi, M. H. Jameel, K. H. Abass, M. Z. H. bin Mayzan and Z. N. Salman, Impact of Electron–Hole Recombination Mechanism on the Photocatalytic Performance of ZnO in Water Treatment: A Review, *J. Sol-Gel Sci. Technol.*, 2024, **110**(3), 792–806, DOI: 10.1007/s10971-024-06385-x.

19 Y. Wang, M. Zhang, H. Ma, H. Su, A. Li, W. Ruan and B. Zhao, Surface Plasmon Resonance from Gallium-Doped Zinc Oxide Nanoparticles and Their Electromagnetic Enhancement Contribution to Surface-Enhanced Raman Scattering, *ACS Appl. Mater. Interfaces*, 2021, **13**(29), 35038–35045, DOI: 10.1021/acsami.1c05804.

20 P. Lad, V. Pathak, A. B. Thakkar, P. Thakor, M. P. Deshpande and S. Pandya, ZnO Nanoparticles Synthesized by Precipitation Method for Solar-Driven Photodegradation of Methylene Blue Dye and Its Potential as an Anticancer Agent, *Braz. J. Phys.*, 2023, **53**(3), 63, DOI: 10.1007/s13538-023-01278-w.

21 E. I. Naik, H. S. B. Naik, M. S. Sarvajith and E. Pradeepa, Co-Precipitation Synthesis of Cobalt Doped ZnO Nanoparticles: Characterization and Their Applications for Biosensing and Antibacterial Studies, *Inorg. Chem. Commun.*, 2021, **130**, 108678, DOI: 10.1016/j.inoche.2021.108678.

22 S. Kanwal, M. Tahir Khan, V. Tirth, A. Algahtani, T. Al-Mughanam and A. Zaman, Room-Temperature Ferromagnetism in Mn-Doped ZnO Nanoparticles Synthesized by the Sol–Gel Method, *ACS Omega*, 2023, **8**(31), 28749–28757, DOI: 10.1021/acsomega.3c03418.

23 A. Ejsmont and J. Goscianska, Hydrothermal Synthesis of ZnO Superstructures with Controlled Morphology via Temperature and pH Optimization, *Materials*, 2023, **16**(4), 1641, DOI: 10.3390/ma16041641.

24 A. Raza, K. Sayeed, A. Naaz, M. Muaz, S. N. Islam, S. Rahaman, F. Sama, K. Pandey and A. Ahmad, Green Synthesis of ZnO Nanoparticles and Ag-Doped ZnO Nanocomposite Utilizing Sansevieria Trifasciata for High-Performance

Asymmetric Supercapacitors, *ACS Omega*, 2024, **9**(30), 32444–32454, DOI: 10.1021/acsomega.3c10060.

25 R. Kalimuthu, K. Meenachi Sellan, D. Antony, S. Rajaprakasam, V. Chokkalingam, P. Chidambaram and S. Kanagarajan, Nanopriming Action of Microwave-Assisted Biofunctionalized ZnO Nanoparticles to Enhance the Growth under Moisture Stress in Vigna Radiata, *ACS Omega*, 2023, **8**(31), 28143–28155, DOI: 10.1021/acsomega.3c01329.

26 A. Das, E. Partyka-Jankowska, M. Zając, A. Hemberg and C. Bittencourt, Impact of Synthesis Parameters upon the Electronic Structure in PVD-Deposited $Cd_xZn_{1-x}O$ Composite Thin Films: An XPS-XANES Investigation, *ACS Omega*, 2024, **9**(8), 9835–9846, DOI: 10.1021/acsomega.4c00892.

27 S. Benchelia, Y. Messai, A. Chetoui and D. E. Mekki, Enhancing Antibacterial Activity through Controlled Ball Milling: Structural, Morphological and Optical Studies of ZnO Nanoparticles, *Nano-Struct. Nano-Objects*, 2024, **39**, 101285, DOI: 10.1016/j.nanoso.2024.101285.

28 N. N. Tarasenka, V. G. Kornev, A. A. Nevar, S. J. Lee, H. M. Maltanava, S. K. Poznyak, M. Y. Choi and N. V. Tarasenko, Synthesis of ZnO/C Nanocomposites via Liquid-Assisted Laser Ablation in an Applied Electric Field for Supercapacitor Applications, *ACS Appl. Nano Mater.*, 2023, **6**(7), 5918–5929, DOI: 10.1021/acsanm.3c00310.

29 N. M. Hosny, I. Gomaa, M. G. Elmahgary and M. A. Ibrahim, ZnO Doped C: Facile Synthesis, Characterization and Photocatalytic Degradation of Dyes, *Sci. Rep.*, 2023, **13**(1), 14173, DOI: 10.1038/s41598-023-41106-4.

30 A. Sun, S. Ma and W.-X. Wang, Two-Sided Cellular and Physiological Effects of Zinc Oxide Nanoparticles (nZnO): A Critical Review, *Environ. Sci. Nano*, 2025, **12**, 1059–1078, DOI: 10.1039/D4EN00676C.

31 V. Amrute, Monika, K. K. Supin, M. Vasundhara and A. Chanda, Observation of Excellent Photocatalytic and Antibacterial Activity of Ag Doped ZnO Nanoparticles, *RSC Adv.*, 2024, **14**(45), 32786–32801, DOI: 10.1039/d4ra05197a.

32 O. Eldahshan, M. Abdelhalim, E. Elsayed and K. Ahmed Saad, GC/Ms Analysis and Antimicrobial Activities of Different Extracts of Egyptian Sprouting Broccoli Leaves (Brassica Oleracea L. Var. Italica) Family Brassicaceae, *Arch. Pharm. Sci. Ain Shams Univ.*, 2023, **7**(1), 31–40, DOI: 10.21608/aps.2023.189998.1107.

33 E. C. Okoli, I. J. Umaru and O. Olawale, Determination of Phytochemical Constituents, Antibacterial and Antioxidant Activities of Ethanolic Leaf Extracts of Pterocarpus Erinaceus, *Biodiversitas J. Biol. Divers*, 2023, **24**(4), 2272, DOI: 10.13057/biodiv/d240440.

34 P. Wu, X. Tang, R. Jian, J. Li, M. Lin, H. Dai, K. Wang, Z. Sheng, B. Chen, X. Xu, C. Li, Z. Lin, Q. Zhang, X. Zheng, K. Zhang, D. Li and W. D. Hong, Chemical Composition, Antimicrobial and Insecticidal Activities of Essential Oils of Discarded Perfume Lemon and Leaves (Citrus Limon (L.) Burm. F.) as Possible Sources of Functional Botanical Agents, *Front. Chem.*, 2021, 9, DOI: 10.3389/fchem.2021.679116.

35 B. Singh, A. Kaushal, I. Bdikin, K. Venkata Saravanan and J. M. F. Ferreira, Effect of Ni Doping on Structural and Optical Properties of $Zn_{1-x}Ni_xO$ Nanopowder Synthesized via Low Cost Sono-Chemical Method, *Mater. Res. Bull.*, 2015, **70**, 430–435, DOI: 10.1016/j.materresbull.2015.05.009.

36 P. Scherrer, Estimation of the Size and Internal Structure of Colloidal Particles by Means of Röntgen, *Nachr Ges Wiss Gött*, 1918, **2**, 96–100.

37 B. D. Cullity and R. Smoluchowski, Elements of X-Ray Diffraction, *Phys. Today*, 1957, **10**(3), 50, DOI: 10.1063/1.3060306.

38 B. Himabindu, N. S. M. P. Latha Devi, G. Sandhya, T. Naveen Reddy, T. Saha, B. Rajini Kanth and Md Sarowar Hossain, Structure Based Photocatalytic Efficiency and Optical Properties of ZnO Nanoparticles Modified by Annealing Including Williamson-Hall Microstructural Investigation, *Mater. Sci. Eng. B*, 2023, **296**, 116666, DOI: 10.1016/j.mseb.2023.116666.

39 D. Balzar and H. Ledbetter, Voigt-Function Modeling in Fourier Analysis of Size- and Strain-Broadened X-Ray Diffraction Peaks, *J. Appl. Crystallogr.*, 1993, **26**(1), 97–103, DOI: 10.1107/S0021889892008987.

40 A. Khorsand Zak, M. W. H. Abd, M. E. Abrishami and R. Yousefi, X-Ray Analysis of ZnO Nanoparticles by Williamson–Hall and Size–Strain Plot Methods, *Solid State Sci.*, 2011, **13**(1), 251–256, DOI: 10.1016/j.solidstatesciences.2010.11.024.

41 S. Sagadevan, K. Pal, Z. Z. Chowdhury and M. E. Hoque, Structural, Dielectric and Optical Investigation of Chemically Synthesized Ag-Doped ZnO Nanoparticles Composites, *J. Sol-Gel Sci. Technol.*, 2017, **83**(2), 394–404, DOI: 10.1007/s10971-017-4418-8.

42 U. Vijayalakshmi, M. Chellappa, U. Anjaneyulu, G. Manivasagam and S. Sethu, Influence of Coating Parameter and Sintering Atmosphere on the Corrosion Resistance Behavior of Electrophoretically Deposited Composite Coatings, *Mater. Manuf. Process.*, 2016, **31**(1), 95–106, DOI: 10.1080/10426914.2015.1070424.

43 G. Murtaza, R. Ahmad, M. S. Rashid, M. Hassan, A. Hussnain, M. A. Khan, M. Ehsan ul Haq, M. A. Shafique and S. Riaz, Structural and Magnetic Studies on Zr Doped ZnO Diluted Magnetic Semiconductor, *Curr. Appl. Phys.*, 2014, **14**(2), 176–181, DOI: 10.1016/j.cap.2013.11.002.

44 J. Tauc, Optical Properties and Electronic Structure of Amorphous Ge and Si, *Mater. Res. Bull.*, 1968, **3**(1), 37–46, DOI: 10.1016/0025-5408(68)90023-8.

45 G. Essalah, G. Kadim, A. Jabar, R. Masrour, M. Ellouze, H. Guermazi and S. Guermazi, Structural, Optical, Photoluminescence Properties and Ab Initio Calculations of New Zn_2SiO_4/ZnO Composite for White Light Emitting Diodes, *Ceram. Int.*, 2020, **46**(8, Part B), 12656–12664, DOI: 10.1016/j.ceramint.2020.02.031.

46 N. L. Tarwal and P. S. Patil, Enhanced Photoelectrochemical Performance of Ag–ZnO Thin Films Synthesized by Spray Pyrolysis Technique, *Electrochim. Acta*, 2011, **56**(18), 6510–6516, DOI: 10.1016/j.electacta.2011.05.001.

47 S. Supothina, P. Seeharaj, S. Yoriya and M. Sriyudthsak, Synthesis of Tungsten Oxide Nanoparticles by Acid Precipitation Method, *Ceram. Int.*, 2007, **33**(6), 931–936, DOI: 10.1016/j.ceramint.2006.02.007.

48 U. Wijesinghe, G. Thiripuranathar, H. Iqbal and F. Menaa, Biomimetic Synthesis, Characterization, and Evaluation of Fluorescence Resonance Energy Transfer, Photoluminescence, and Photocatalytic Activity of Zinc Oxide Nanoparticles, *Sustainability*, 2021, **13**(4), 2004, DOI: 10.3390/su13042004.

49 B. C. Nwaiwu, E. E. Oguzie and C. C. Ejiogu, Photocatalytic Degradation of Congo Red Using Doped Zinc Oxide Nanoparticles, *Int. J. Environ. Qual.*, 2024, **60**, 18–26, DOI: 10.6092/issn.2281-4485/18803.

50 L. Hamza, S. E. Laouini, H. A. Mohammed, S. Meneceur, C. Salmi, F. Alharthi, S. Legmairi and J. A. A. Abdullah, Biosynthesis of ZnO/Ag Nanocomposites Heterostructure for Efficient Photocatalytic Degradation of Antibiotics and Synthetic Dyes, *Z. Physiol. Chem.*, 2024, **238**(9), 1599–1622, DOI: 10.1515/zpch-2023-0379.

51 K. T. C. Cheah and J. Y. Sum, Synthesis and Evaluation of Fe-Doped Zinc Oxide Photocatalyst for Methylene Blue and Congo Red Removal, *Prog. Energy Environ.*, 2022, 13–28, DOI: 10.37934/progee.22.1.1328.

52 W. Bao, X. Fu, K. Hu and Y. Zhao, Adsorption and Photo-Catalytic Properties of Congo Red by Cobalt Doped Porous ZnO Prepared Through Hydrothermal Method, *E3S Web Conf.*, 2020, **185**, 04048, DOI: 10.1051/e3sconf/202018504048.

53 S. Ghaffar, A. Abbas, M. Naeem-ul-Hassan, N. Assad, M. Sher, S. Ullah, H. A. Alhazmi, A. Najmi, K. Zoghebi, M. Al Bratty, A. Hanbashi, H. A. Makeen and H. M. A. Amin, Improved Photocatalytic and Antioxidant Activity of Olive Fruit Extract-Mediated ZnO Nanoparticles, *Antioxidants*, 2023, **12**(6), 1201, DOI: 10.3390/antiox12061201.

54 N. Assad, A. Abbas, M. F. U. Rehman and M. Naeem-ul-Hassan, Photo-Catalytic and Biological Applications of Phyto-Functionalized Zinc Oxide Nanoparticles Synthesized Using a Polar Extract of Equisetum Diffusum D, *RSC Adv.*, 2024, **14**(31), 22344–22358, DOI: 10.1039/D4RA03573A.

55 A. B. Siddique, M. A. Shaheen, A. Abbas, Y. Zaman, M. A. Bratty, A. Najmi, A. Hanbashi, M. Mustaqeem, H. A. Alhazmi, Z. U. Rehman, K. Zoghebi and H. M. A. Amin, Thermodynamic and Kinetic Insights into Azo Dyes Photocatalytic Degradation on Biogenically Synthesized ZnO Nanoparticles and Their Antibacterial Potential, *Heliyon*, 2024, **10**(23), e40679, DOI: 10.1016/j.heliyon.2024.e40679.

56 K. Pradeev Raj, K. Sadaiyandi, A. Kennedy, S. Sagadevan, Z. Z. Chowdhury, M. R. B. Johan, F. A. Aziz, R. F. Rafique, R. Thamiz Selvi and R. Rathina Bala, Influence of Mg Doping on ZnO Nanoparticles for Enhanced Photocatalytic Evaluation and Antibacterial Analysis, *Nanoscale Res. Lett.*, 2018, **13**(1), 229, DOI: 10.1186/s11671-018-2643-x.

57 T. Deshwal, P. Kumar, S. Ahlawat, S. Kumar, H. Kaur, A. Kumar and A. Kumar, Tailoring Band Gap and Photocatalytic Activity of ZnO via Cu Doping for Enhanced Congo Red Degradation, *Research Square*, 2024, DOI: 10.21203/rs.3.rs-4258505/v1.

58 S. Senthilkumar and K. Govindasamy, Enhancing Photocatalytic Activity of Mn-Doped Zno Nanoparticles Synthesized by Using Novel Ipomoea Staphylina Leaf Extract, *Social Science Research Network: Rochester*, NY, 2023, DOI: 10.2139/ssrn.4675837.

59 N. Elamin, A. Modwi, M. A. B. Aissa, K. K. Taha, O. K. Al-Duaij and T. A. Yousef, Fabrication of Cr–ZnO Photocatalyst by Starch-Assisted Sol–Gel Method for Photodegradation of Congo Red under Visible Light, *J. Mater. Sci. Mater. Electron.*, 2021, **32**(2), 2234–2248, DOI: 10.1007/s10854-020-04988-y.

60 N. J. Tamanna, M. S. Hossain, S. Tabassum, N. M. Bahadur and S. Ahmed, Easy and Green Synthesis of Nano-ZnO and Nano-TiO_2 for Efficient Photocatalytic Degradation of Organic Pollutants, *Heliyon*, 2024, **10**(17), e37469, DOI: 10.1016/j.heliyon.2024.e37469.

61 H. Aliah, N. Puspita Rini, I. Syafar Farouk, Zurnansyah, L. Jestha Mahardhika, P. Dwi Jayanti, H. Perdana Kusumah, R. Marsel Tumbelaka, N. Imani Istiqomah, N. Sumawati Asri, R. Nur Iman and E. Suharyadi, Microstructures, Optical, Magnetic Properties, and Photocatalytic Activity of Magnetically Separable and Reusable ZnO-Doped Fe_3O_4/rGO Nanocomposite Synthesized via Green Route, *Carbon Resour. Convers.*, 2024, **7**(4), 100235, DOI: 10.1016/j.crcon.2024.100235.

62 A. V. Petukhov, Effect of Molecular Mobility on Kinetics of an Electrochemical Langmuir-Hinshelwood Reaction, *Chem. Phys. Lett.*, 1997, **277**(5), 539–544, DOI: 10.1016/S0009-2614(97)00916-0.

63 E. Kusvuran, A. Samil, O. M. Atanur and O. Erbatur, Photocatalytic Degradation Kinetics of Di- and Tri-Substituted Phenolic Compounds in Aqueous Solution by TiO_2/UV, *Appl. Catal. B*, 2005, **58**(3), 211–216, DOI: 10.1016/j.apcatb.2004.11.023.

64 A. W. Khan, N. S. Lali, F. Y. Sabei, M. I. Irfan, M. Naeem-ul-Hassan, M. Sher, A. Y. Safhi, A. Alsalhi, A. H. Albariqi, F. Kamli, H. M. A. Amin and A. Abbas, Sunlight-Assisted Green Synthesis of Gold Nanocubes Using Horsetail Leaf Extract: A Highly Selective Colorimetric Sensor for Pb^{2+}, Photocatalytic and Antimicrobial Agent, *J. Environ. Chem. Eng.*, 2024, **12**(3), 112576, DOI: 10.1016/j.jece.2024.112576.

65 H. Ma, P. L. Williams and S. A. Diamond, Ecotoxicity of Manufactured ZnO Nanoparticles – A Review, *Environ. Pollut.*, 2013, **172**, 76–85, DOI: 10.1016/j.envpol.2012.08.011.

66 H. Moradpoor, M. Safaei, H. R. Mozaffari, R. Sharifi, M. M. Imani, A. Golshah and N. Bashardoust, An Overview of Recent Progress in Dental Applications of Zinc Oxide Nanoparticles, *RSC Adv.*, 2021, **11**(34), 21189–21206, DOI: 10.1039/D0RA10789A.

67 A. M. El Shahawi, Incorporation of Zinc Oxide Nanoparticles and It's Antibacterial Effect on Toothpaste, *Bull. Natl. Res. Cent.*, 2023, **47**(1), 2, DOI: 10.1186/s42269-022-00975-x.

68 T. (Dorothy) Piluk, G. Faccio, S. Letsiou, R. Liang and M. Freire-Gormaly, A Critical Review Investigating the Use

of Nanoparticles in Cosmetic Skin Products, *Environ. Sci. Nano*, 2024, **11**(9), 3674–3692, DOI: **10.1039/D4EN00489B**.

69 R. Gomathi and D. Paradesi, Antibacterial Efficacy of a Topical Skin Cream Loaded with Nano Zinc Oxide, Cetylpyridinium Chloride and Chlorhexidine Gluconate, *Mater. Today Proc.*, 2023, **93**, 54–60, DOI: **10.1016/j.matpr.2023.10.001**.

70 S. Sivakumar, Y. Robinson and N. A. Mala, Studies on Photocatalytic Performance and Supercapacitor Applications of Undoped and Cu-Doped ZnO Nanoparticles, *Appl. Surf. Sci. Adv.*, 2022, **12**, 100344, DOI: **10.1016/j.apsadv.2022.100344**.

71 A. Chauhan, R. Verma, S. Kumari, A. Sharma, P. Shandilya, X. Li, K. M. Batoo, A. Imran, S. Kulshrestha and R. Kumar, Photocatalytic Dye Degradation and Antimicrobial Activities of Pure and Ag-Doped ZnO Using Cannabis Sativa Leaf Extract, *Sci. Rep.*, 2020, **10**(1), 7881, DOI: **10.1038/s41598-020-64419-0**.

72 S. Roguai and A. Djelloul, Structural, Microstructural and Photocatalytic Degradation of Methylene Blue of Zinc Oxide and Fe-Doped ZnO Nanoparticles Prepared by Simple Coprecipitation Method, *Solid State Commun.*, 2021, **334–335**, 114362, DOI: **10.1016/j.ssc.2021.114362**.

73 L. S. Alqarni, A. M. Alghamdi, N. Y. Elamin and A. Rajeh, Enhancing the Optical, Electrical, Dielectric Properties and Antimicrobial Activity of Chitosan/Gelatin Incorporated with Co-Doped ZnO Nanoparticles: Nanocomposites for Use in Energy Storage and Food Packaging, *J. Mol. Struct.*, 2024, **1297**, 137011, DOI: **10.1016/j.molstruc.2023.137011**.

74 V. Do Truc, T. V. Nguyen, T. V. Vu, T. A. Nguyen, T. D. Ngo, T. L. Le, L. P. Thi and T. D. Lam, Zno-Ag Hybrid Nanoparticles Used in the Antimicrobial Solvent-Based Coatings: Antibacterial Studies in the Darkness and Under Visible-Light Irradiation, *Social Science Research Network: Rochester*, NY, 2022, DOI: **10.2139/ssrn.4246711**.

75 A. Ziashahabi, M. Prato, Z. Dang, R. Poursalehi and N. Naseri, The Effect of Silver Oxidation on the Photocatalytic Activity of Ag/ZnO Hybrid Plasmonic/Metal-Oxide Nanostructures under Visible Light and in the Dark, *Sci. Rep.*, 2019, **9**(1), 11839, DOI: **10.1038/s41598-019-48075-7**.

76 J. M. Wu and W. T. Kao, Heterojunction Nanowires of $Ag_xZn_{1-x}O$–ZnO Photocatalytic and Antibacterial Activities under Visible-Light and Dark Conditions, *J. Phys. Chem. C*, 2015, **119**(3), 1433–1441, DOI: **10.1021/jp510259j**.